www.adeepakpublishing.com

Aguilar-Nadalini et al. (2023): JoSS, Vol. 12, No. 02, pp. 1201–1229
(Peer-reviewed article available at www.jossonline.com)

www. JoSSonline.com

Design and On-Orbit Performance of the Electrical Power System for the Quetzal-1 CubeSat

Aldo Aguilar-Nadalini, Kuk H. Chung, Cecilia Marsicovetere, José A. Bagur, Juan F. Medrano, Emilio Miranda, Víctor Ayerdi, Luis Zea
Universidad del Valle de Guatemala
Guatemala City, Guatemala

Abstract

Quetzal-1, a 1U CubeSat developed by the Universidad del Valle de Guatemala (UVG), operated on orbit from April to November of 2020. It included an in-house developed Electrical Power System (EPS) that supplied power to the other systems of the satellite. The EPS incorporated six non-deployable solar panels coupled to three maximum-power point tracking chargers to generate power. A centralized EPS architecture was implemented with 3.3 V, 5 V, and 7.6 V rails used to power up the satellite's systems, all distributed from a central, unregulated power line connected to a rechargeable 4.2 V Li-ion battery. The system also incorporated protection circuitry against fault conditions, a battery heater, and deployment switches to activate the satellite after deployment from the International Space Station (ISS). This manuscript presents the design specifications of the EPS, as well as offering a detailed account of the system's operation on orbit. The EPS ensured a positive power budget throughout the satellite's mission, generating enough power to meet the satellite's demand and keeping the battery recharged regardless of the operating conditions. The system was able to remain power positive even at times when the solar panels' efficiency naturally decreased due to an increase in their superficial temperature during high beta angle seasons with no eclipse. Furthermore, the on-board heater prevented battery freezing even during maximum eclipse conditions. This paper also includes design recommendations, as well as open-source circuit schematics of the EPS that may be valuable to other teams working on future CubeSat missions.

---

1. Introduction

Quetzal-1 (ket-sahl-oo-noh) was a 1U CubeSat developed by Universidad del Valle de Guatemala (UVG) and supported, in terms of its launch to and deployment from the International Space Station (ISS), by the United Nations Office for Outer Space Affairs (UNOOSA) and the Japan Aerospace Exploration Agency (JAXA) under their joint KiboCUBE Programme (Taniguchi et al., 2020). Quetzal-1's mission was selected via a methodology based on maximizing benefits while considering programmatic risk and technical feasibility (Zea et al., 2016). The satellite's

Corresponding Author: Luis Zea – lpzea@uvg.edu.gt / Víctor Ayerdi – vhayerdi@uvg.edu.gt

Publication History: Submitted – 10/30/21; Revision Accepted – 02/17/22; Published – 05/31/23

technical mission was to test a multispectral imaging system capable of acquiring images at different wavelengths by rotating a carousel carrying four light filters in front of a monochromatic camera. The systems engineering approaches implemented on this project are described by Martinez et al. (2018), the multispectral payload by Zea et al. (2023), the Attitude Determination and Control System (ADCS) by Álvarez et al. (2023), the structure's Finite Element Analysis by Birnie et al. (2023), and the Command & Data Handling System (CDHS) by Chung et al. (2023).

The design of the Electrical Power System (EPS) was based on four main criteria to provide mission success while operating in space. First, the EPS was tasked with generating enough power to meet the satellite's demand on orbit using photovoltaic cells. Second, the EPS was also tasked with storing the generated power on a Li-ion rechargeable battery to allow the continuity of operations when the satellite was in eclipse. Third, the module was tasked with the conditioning and distribution of power within the satellite's systems. Finally, it was tasked with protecting the other systems from power malfunctions. The EPS was developed in-house due to budgetary constraints, and it was designed according to the requirements stated in the JEM Payload Accommodation Handbook (JAXA, 2018). The design and development of the EPS are detailed in Section 2, on-orbit results are presented in Section 3, and conclusions and recommendations are given in Sections 4 and 5, respectively.

2. Design and Development

A centralized architecture was implemented for the EPS system of the satellite with 3.3 V, 5 V, and 7.6 V rails. All rails were distributed from a central, unregulated power line that was connected to the output of three solar chargers and to the satellite's Li-ion battery, which drove the line's voltage at 3.2 - 4.2 V. Figure 1 shows the high-level diagram of the system. The EPS was divided into three main subsystems: energy harvesting, energy storage, and energy distribution. This section details the purpose of each EPS subsystem as well as the rationale behind the selection of the components that comprised each of these subsystems. The key requirements that drove the EPS design can be found in Table D1.

2.1. Energy Harvesting

Quetzal-1 carried 11 solar cells to generate the power required for operations and to recharge the battery aboard the satellite, which guaranteed continuity of operations during eclipse. A passive magnetic ADCS was implemented on the satellite; thus, a non-zero roll was expected over the satellite's uncontrolled axis that was aligned with Earth's magnetic field lines

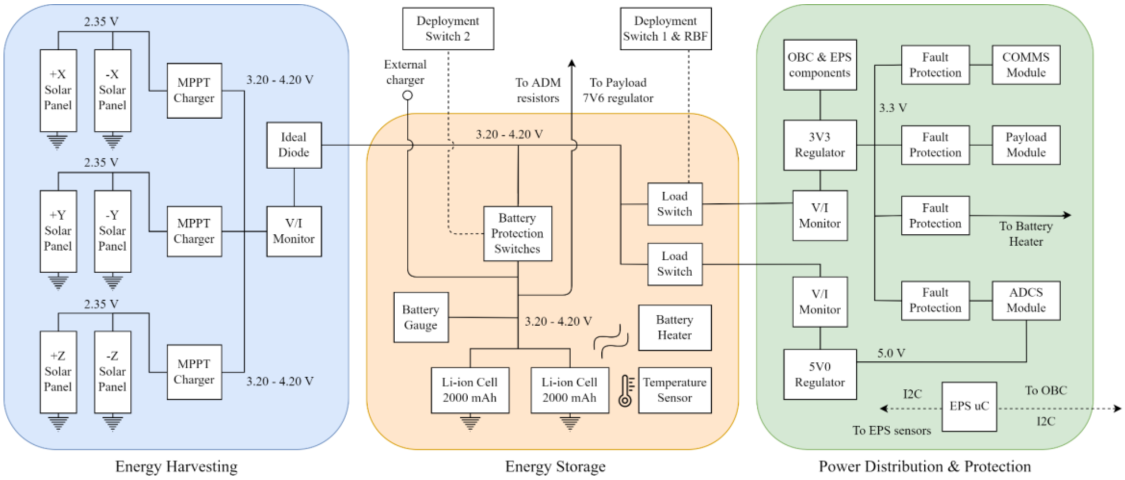
2.35 V
+X Solar Panel
-X Solar Panel
MPPT Charger
3.20 - 4.20 V
2.35 V
+Y Solar Panel
-Y Solar Panel
MPPT Charger
2.35 V
+Z Solar Panel
-Z Solar Panel
MPPT Charger
3.20 - 4.20 V
Ideal Diode
V/I Monitor
Deployment Switch 2
External charger
To ADM resistors
To Payload 7V6 regulator
Deployment Switch 1 & RBF
3.20 - 4.20 V
Battery Protection Switches
Load Switch
Load Switch
Battery Gauge
3.20 - 4.20 V
Battery Heater
Li-ion Cell 2000 mAh
Li-ion Cell 2000 mAh
Temperature Sensor
OBC & EPS components
Fault Protection
COMMS Module
3.3 V
3V3 Regulator
Fault Protection
Payload Module
V/I Monitor
Fault Protection
To Battery Heater
V/I Monitor
Fault Protection
ADCS Module
5.0 V
5V0 Regulator
I2C
EPS uC
To OBC
I2C
To EPS sensors
Energy Harvesting
Energy Storage
Power Distribution & Protection

Figure 1. Quetzal-1's electrical power system architecture (solid lines – power; dotted lines – digital).

(Alvarez et al., 2023). For this reason, six in-house developed non-deployable panels were placed over each face of the 1U CubeSat to ensure continuous power generation regardless of the satellite's orientation towards the Sun (see Figure A1). Five of the panels carried two photovoltaic cells (AzurSpace, Cat. No. 3G30A) each in a parallel configuration to harvest solar energy. The bottom panel of the satellite only carried a single cell because the payload's camera boresight occupied half of that panel (Zea et al., 2023). This design was preferred over pre-made commercial solutions because of its lower cost and because the characteristics of the 3G30A cells met the power requirements of the satellite (maximum voltage and current, efficiency, and operating temperature range) (AzurSpace, 2016).

The parallel configuration of the 3G30A cells allowed each panel to operate at 2.35 V with a maximum output current of 1 A. This configuration prevented a complete panel malfunction in case one of the two cells in a panel ceased to operate nominally in space. Three low voltage step-up converters (STMicroelectronics, Cat. No. SPV1040), each coupled to a pair of opposite panels (as shown in Figure 1), were implemented to reach the charging voltage of the satellite's Li-ion battery (4.20 V). This converter model was selected because it operated as a maximum-power point tracking (MPPT) solar battery charger using a Perturb & Observe algorithm (P&O) to track the maximum-power point of the cells. It also implemented a Constant Current - Constant Voltage (CCCV) algorithm to limit its output power when the battery neared full charge to avoid overcharge and preserve battery health (Microelectronics, 2011). Furthermore, this converter model was also selected because it had flight heritage from the ESTCube-1 mission (Pajusalu et al., 2012).

Ground tests were performed to evaluate the efficiency of the solar cells and chargers coupled together. The panels were placed on a static environment parallel to the ground facing directly at the Sun, as shown in Figure 2. The irradiance was typically 940 W/m^2 during the tests, as measured by a pyranometer. Power measurements performed on the input and output of the solar chargers indicated that they were operating with an average efficiency of 88.02% ± 0.25% (95% confidence interval). The cells' efficiency was also calculated by measuring the power at the output of the solar panels. The resulting cell efficiency was 21.79% ± 0.06%, which was lower than the 29.3% efficiency indicated by the cells' manufacturer. The reduced cell efficiency was most likely the result of the solar panels being encased in acrylic boxes for protection rather than directly under the Sun during the tests. Furthermore, it was observed that an increase in the surface temperature of the panels during the tests also led to reduced cell efficiency (data not shown).

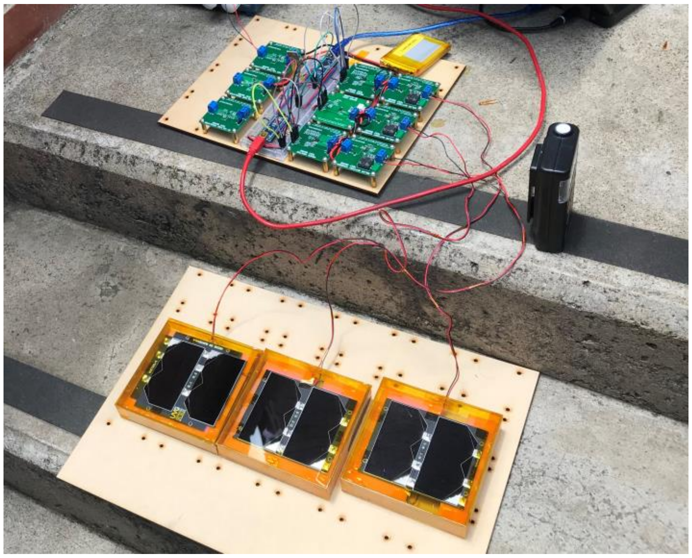

Figure 2. Ground tests to evaluate the solar cells' and chargers' efficiency.

2.1.1. Estimation of the Power Generated by the Entire Energy Harvesting Subsystem

A methodology to calculate the mean cross-sectional area of a tumbling CubeSat using a composite flat-plate model is presented in Oltrogge and Leveque (2011). This same methodology was used to calculate the average surface area of Quetzal-1 that would be illuminated by the Sun perpendicularly (at a solar incidence angle of 0°) and would be generating power at a given time while the satellite uniformly rotated in space. An approximation of the average power generated by the entire energy harvesting subsystem could be calculated using this estimated area. The area of two solar cells (6.036×10^{-3} m^2) was used as the surface area of the three visible sides of the rotating cube in the flat-plate model equation. This resulted in a mean cross-sectional area of 9.054 x 10^{-3} m^2. Subsequently, the average power generated by the entire harvesting subsystem in sunlight was estimated at 2.37 W, assuming that the cells' efficiency was going to be 21.79% and the solar chargers' efficiency was going to remain at 88.02% in space, as measured in the tests. This average power was estimated considering that the Sun's irradiance on orbit is 1366.1 W/m^2 (ASTM, 2014).

2.1.2. Solar Panel Protections

As mentioned before, each pair of opposite panels was connected in parallel to a single solar charger, reducing the number of chargers needed aboard the satellite. Ideal blocking diodes (ON Semiconductor, Cat. No. MBR120VLSFT-3G) were implemented at the positive terminal of each panel to prevent reverse currents when one of the panels in the pair (e.g., +X) received sunlight and the other panel (e.g., -X) was in shadow. Additionally, a general ideal blocking diode (Linear Tech., Cat. No. LTC4352) was implemented between the chargers' node and the battery node (as shown in Figure 1) to prevent reverse quiescent currents flowing from the battery to the chargers' peripheral circuitry during eclipse. Quiescent currents flowing from the battery to the energy harvesting subsystem could severely damage the Li-ion cells due to deep discharge during storage prior to deployment or during the mission (Arnold et al., 2012). Finally, a V/I monitor (Texas Instruments, Cat. No. INA260), referenced as Solar Channel Monitor or SCM throughout this paper, was placed between the chargers' output and the blocking diode to measure the generated power at the output of the energy harvesting subsystem. The subsystem's circuit schematics are shown in Figures B1-3.

2.2. Energy Storage

2.2.1. On-board Battery Characteristics

The satellite carried a rechargeable battery to store the energy generated by the solar panels. This battery was essential to guarantee continuous power supply during eclipse periods and during peak power consumption when the panels could not meet the full power demand of the satellite. Quetzal-1's battery was composed of two 3.7 V lithium-ion polymer battery cells (DataPower, Cat. No. Dtp 605068), with 2000 mAh capacity each, connected in parallel (DataPower, 2018). Li-ion cells were preferred over other commercial alternatives due to their smaller size and higher energy density. This model was selected because its characteristics matched those of the SparkFun PRT-08483 cells used in the Colorado Student Space Weather Experiment (CSSWE) mission (Li et al., 2012) (see Table C1).

The battery cells incorporated a protection circuit as a safeguard against internal shorts, external shorts, overcharge (voltages above 4.28 V), and overdischarge (voltages below 3.0 V). These cells had a maximum discharge current of 2 A each; thus, they could provide a maximum current of 4 A to the satellite in a parallel configuration, and their operating voltage range was adequate to feed the three implemented voltage rails (DataPower, 2018). Sixteen battery cells were subjected to a variety of tests, including vacuum leak tests, random vibration tests, thermal tests, and charge-discharge tests as part of the ISS flight battery cell certification and selection process. The cells successfully passed all the tests (see Tables E1-2) according to the acceptance criteria detailed in NASA (2017), and two of the cells were arbitrarily selected as the flight battery.

2.2.2. Battery Thermal Management

Li-ion cells can only be discharged at temperatures between -20°C and 60°C, and charged at temperatures between 0°C and 45°C, per the manufacturer's specifications. Charging Li-ion cells at temperatures below freezing point can lead to lithium plating of the graphite electrode of the battery, which in turn leads to battery performance degradation and cell safety issues (Petzl et al., 2015). For this reason, an on-board battery heater was implemented to always keep the battery above 0°C. The selected battery heater was a 13-Ω Kapton heater resistor (Heat Specific, Cat. No. Rectangular-L30W20 mm). This heater model was selected because its resistance value restricted the heater's power demand to less than 1 W at 3.3 V, and its dimensions were adequate for it to be placed between the two stacked cells of the battery. The stack was wrapped with one-sided Kapton tape to further insulate the battery (see Figure A2). The location of the EPS board (and battery stack) inside the satellite can be appreciated in Figure A3.

A thermal sensor (Texas Instruments, Cat. No. TMP100-Q1) was placed on top of the battery stack (see Figure A2) to monitor its temperature and determine if the thermal conditions were adequate and thus enabled an optimal battery state of health. The sensor transmitted the measured temperature to the microcontroller (μC) on the EPS circuit board, which in turn relayed the information to the onboard computer (OBC). The OBC was programmed to command the activation of the battery heater when the battery temperature dropped below 3°C, and its deactivation when the temperature rose above 5°C. This hysteresis loop was established experimentally through thermal tests of the battery with the heater, which indicated that this configuration would keep the battery above 0°C on orbit (data not shown). The battery heater could also be operated manually via ground control station (GCS) commands when needed. Furthermore, a heater emergency mode was programmed into the OBC in case the thermal sensor failed on orbit. If the EPS failed to send the battery temperature back to the OBC, the OBC would command the heater to periodically cycle between its on and off states, with the duration of each state defined by a set of two heater cycle time parameters modifiable via GCS commands.

2.2.3. Battery Fuel Gauging

A battery gauge (Texas Instruments, Cat. No. BQ27441-G1) was implemented for fuel gauging the Li-ion cells on board the satellite. It measured battery voltage, average current, average power, remaining capacity, state of charge, and state of health (Texas Instruments, 2013). This component was chosen because it required minimal user configuration and could be powered up directly from the battery. It could also operate at temperatures between -40°C and 85°C, and ground tests indicated that the sensor could operate nominally under vacuum conditions (data not shown), making it adequate for on-orbit operations. This particular battery gauge model was designed to gauge a single Li-ion cell. However, it was used to gauge two 2000 mAh Li-ion cells in a parallel configuration, and it was programmed to gauge them as a single 4000 mAh cell.

During ground tests, it was observed that the battery monitor would sporadically measure an incorrect battery state of charge (SOC). It was hypothesized that these glitches were caused by incorrect measurement of the parallel cells' internal resistance due to being interpreted as a single cell by the monitor. Nevertheless, the overall performance of the sensor was deemed adequate for flight. To avoid any runtime error due to the SOC glitches, redundancy for this measurement was implemented via the following equation:

$$SOC_{estimate} = 113.69 \cdot Voltage_{Main} - 372.08. \quad (1)$$

This equation was derived by performing a charging cycle of the battery at 400 mA (standard charging current for battery model – see Table C1) and determining a linear relationship between battery SOC and the voltage of the satellite's main power bus. The equation was implemented on the OBC's software so it could estimate the charge of the battery even when the battery gauge returned incorrect readings. This model had its limitations because the SOC of a Li-ion battery is related to its open-circuit voltage (OCV), and the voltage of the main power bus corresponded to the sum of the OCV and the voltage drop across the battery's internal resistance due to battery current. This model was determined experimentally and proved to be adequate for Quetzal-1's operations, but the authors recommend including the effects of battery current when designing SOC estimation models.

2.2.4. Battery Protection Switches

Two power switches (Texas Instruments, Cat. No. TPS2557) were implemented on a back-to-back configuration to be able to switch on and off the charge and discharge paths of the battery. This configuration has flight heritage from the ESTCube-1 mission, where it was successfully used to protect the battery (Pajusalu et al., 2012). The enable pin of the discharge path switch was connected to a deployment switch (Honeywell, Cat. No. ZM50E70J01) that kept the battery disconnected prior to deployment, following requirements from JAXA (JAXA, 2018). The discharge path switch was configured to automatically limit the battery discharge current to a maximum of 3.35 A, and the charge path power switch was configured to limit the battery charge current to a maximum of 1.00 A. The schematics of the battery protection and deployment switch circuits are shown in Figures B4 and B5, respectively.

2.3. Power Distribution & Protection

2.3.1. Power Conditioning

As previously mentioned, three regulated voltage buses were implemented to power up the components used on each of the satellite's systems. As a design requirement, the Gomspace's Nanomind (A3200) and Nanocom (AX100), used as the satellite's OBC and Communications System (COMMS) transponder, respectively, needed a 3.3 V bus to be powered up. For design simplicity, most of the integrated circuits and components implemented on the EPS, Payload, and ADCS circuit boards were also chosen to operate at this voltage. The only exceptions were two low dropout 3.3 V references (Texas Instruments, Cat. No. LM4120) implemented on the ADCS module, which operated at 5 V, and a piezoelectric motor (Tekceleo, Cat. No. WLG-30) that operated at 7.6 V.

The 3.3 V references were implemented on the ADCS board to generate a stable 3.3 V reference voltage required by two I2C system monitors (Texas Instruments, Cat. No. ADC128D818). These monitors were in charge of measuring the voltage output of each of the 12 photodiodes (Vishay, Cat. No. TEMD6010FX01) placed on the satellite's panels as part of the ADCS (Alvarez et al., 2023). The piezoelectric motor was part of the Payload system, and it was tasked with rotating the filter carousel aboard the satellite. Individual 5 V and 7.6 V buses were implemented apart from the main 3.3 V power bus to power up the 3.3 V voltage references and the motor, respectively. Voltage levels for each bus were generated using voltage regulators connected to the central unregulated 4.2 V power line and are detailed in Table 1. The 4.2 V power line was in turn connected to the positive terminal of Quetzal-1's Li-ion battery and the power output of the solar chargers, as shown in Figure 1. Four 5.6 Ω resistors (Yageo, Cat. No. MFR50SFTE52-5R6) that were part of the antenna deployment mechanism were also connected directly to the 4.2 V power line.

Each regulator was selected by taking into account the peak power consumption that the components connected to each bus could reach. The total current consumption through the 3.3 V bus could only reach 1.3 A (less than the TPS63070's maximum of 2 A) if all components connected to it were operating under peak conditions. The TPS61089 converter proved adequate for powering up the WLG-30 piezoelectric motor implemented on the Payload system, which could demand a maximum of 1.2 A through the 7.6 V bus. Lastly, the maximum current output of 150 mA of the 5 V regulator was enough to supply the power demand of the ADCS LM4120 voltage references.

2.3.2. Protection and Monitoring of the 3.3 V and 5 V Buses

To keep the satellite's battery and solar chargers safe from any overcurrent or short-circuit condition on the load side, two power-distribution switches (Texas Instruments, Cat. No. TPS2551) were implemented: one between the unregulated 4.2 V power line and the input of the 3.3 V regulator, and another between the

Table 1. Electrical Characteristics of the Implemented Voltage Regulators (Texas Instruments, 2016a, b; Microchip, 2014)

Voltage	Regulator	Type	Input Voltage	Max Out Current	Efficiency	Temp. Range
3.3 V	Texas Instruments, TPS63070	Buck-boost	2.0 – 16 V	2 A	90%	-40 – 125°C
7.6 V	Texas Instruments, TPS61089	Boost	2.7 – 12 V	10 A	95%	-40 – 125°C
5.0 V	Microchip Tech., MCP1252	Charge pump (buck-boost)	2.1 – 5.5 V	150 mA	68%	-40 – 125°C

4.2 V line and the input of the 5 V regulator, as shown in Figure 1. Both switches were calibrated to automatically limit the load current to a maximum of 1.6 A. Additionally, the enable pin of the 3.3 V bus protection switch was connected to the satellite's remove before flight (RBF) switch, as well as to one of its two deployment switches (Honeywell, Cat. No. ZM50E70J01). This was done to disconnect the 3.3 V bus from the 4.2 V power line if one of these switches were activated, as per the deployer specifications (JAXA, 2018).

V/I monitors (Texas Instruments, Cat. No. INA260) were implemented between the power-distribution switches and each regulator (see Figure 1) to measure voltage and current at the input of the converters. The monitor for the 3.3 V bus is referenced as the Main Bus monitor (MBM) from this point on, and the one for the 5 V bus is referenced as the Secondary Bus monitor (SBM). The voltage measured by the monitors provided a rough estimate of the battery's state of charge, and the measured current was essential to determine if the satellite was demanding a nominal amount of power from the solar panels and the battery. These monitors, as well as all the other EPS sensors, were connected via I2C to a microcontroller (Microchip, Cat. No. ATMEGA328P) that was in charge of retrieving data from the sensors and relaying it to the OBC. The EPS flight software is available online at (Quetzal-1 Team, 2021).

2.3.3. Protection of the 7.6 V Bus

The TPS61089 converter incorporated protection against overcurrent on the 7.6 V bus, eliminating the need for a power-distribution switch between the battery and its input. The converter was calibrated to limit its output current to a maximum of 9.36 A. The TPS61089 also incorporated a digital enable pin that could shut down the device when a logic low level was present on the pin. Since the converter was placed directly on the payload circuit board rather than on the main EPS board, the converter's enable pin was connected to the payload µC. This simplified software design, transferring control of the converter directly to the payload µC, which also operated the motor and the camera. The circuit schematics for this and the other regulators can be found in Figures B6 to B8.

2.3.4. Fault Protection Boards

Aside from the overcurrent and short-circuit protections implemented in each regulator, individual protections were implemented for each of the satellite's systems. Fault protection boards (FPB) were placed on the EPS circuit board between the 3.3 V regulator and the individual power buses for each system. The FPBs were made up of two components connected in series: a power-distribution switch (Texas Instruments, Cat. No. TPS2551) and a high-side unipolar current shunt monitor (Texas Instruments, Cat. No. INA169). The switches' purpose was twofold: to protect the main 3.3 V power bus from any overcurrent or short-circuit condition on a specific system, and to power up or power down a specific system according to the enable signals sent by the EPS µC. For example, if the OBC instructed the EPS µC to activate the Payload system, a logical high signal was sent from a digital pin of the EPS µC to the enable pin of the TPS2551 switch on the payload FPB. Each FPB switch was calibrated to automatically limit the maximum allowed current according to each system's consumption. The ADCS and Payload systems, as well as the battery heater, were limited to a max current of 700 mA. The COMMS system was limited to a max current of 1.6 A, in line with the AX100 transceiver power ratings.

The INA169 current monitors were used to measure the current consumption of each individual system. All INA169 monitors were connected to an analog pin of the EPS µC, which was tasked with processing and forwarding the measured current data to the OBC. I2C isolators (Texas Instruments, Cat. No. TCA4311A) were implemented on every system's circuit board to isolate the modules from the main I2C communication bus when the FPBs powered them down following the OBC's commands or due to a detected failure. This avoided I2C bus pull-downs caused by unpowered slaves. The schematics for the FPBs are shown in Figures B9-10, and for the I2C isolators in Figure B11.

2.4. Power Budget

The power budget for Quetzal-1 was calculated using datasheet ratings for each component implemented on the satellite's circuit boards. Ground tests were also performed to assess the power consumption of each system. Two main power modes were established for the satellite, the battery heater's duty cycle being the only difference between them. During ground tests, it was unknown how the battery temperature would fluctuate on orbit due to periods of sunlight and eclipse; therefore, the heater's duty cycle could not be empirically determined. The two calculated scenarios were: OP-MODE 1 where the heater was assumed to be inactive during all of the orbit, and OP-MODE 2 where the heater was operating for a third of the orbit, as shown in Table 2. This assumption was based on the estimation that the eclipse duration for the satellite, placed in a circular 400-km high LEO orbit, was going to be approximately a third of each orbit, following the methodology described in (Sumanth, 2019). A 10% margin was added to every calculation to account for voltage regulator losses, power line losses, and possible regulator efficiency degradation in space.

A special power consumption scenario was also considered to account for the activation of the Payload system on orbit. The Payload system included the payload circuit board, an Arducam 5MP Plus OV5642, and the WLG-30 piezoelectric motor. The activation of the Payload system for the execution of a full operation (picture capture and download) typically lasted 225 s and caused a 123 mW increase in the total power demanded by the satellite during an orbit (Zea et al., 2023).

As detailed in subsection 2.1, the power that the energy harvesting subsystem would generate in space when in sunlight was estimated to be approximately 2.37 W. Assuming that the satellite would be under sunlight conditions for two thirds of the orbit, the average power generated per orbit was estimated by multiplying 2.37 W * 66.67% = 1.58 W. Note that the estimated generated power per orbit was greater than the highest estimate of power consumption OP-MODE 2 + payload activation (0.996 W + 0.123 W = 1.12 W). The resulting factor of safety was 1.58/1.12 = 1.41, which indicated that the satellite was going to have a positive power budget on orbit, allowing the battery to recharge.

3. On-Orbit Results

3.1. Energy Harvesting

3.1.1. Power Generation Depending on Temperature and Battery State of Charge

As mentioned in subsection 2.1, there were two main factors that had a direct effect on the amount of power generated by the energy harvesting subsystem: the operating temperature of the solar cells and the state of charge of the battery. No thermal sensors were placed directly on the exterior of the satellite's panels to measure the surface temperature of the solar cells on orbit; however, three thermal sensors located around the satellite proved to be useful in detecting internal temperature fluctuations during on-orbit operations. The first sensor was placed over the battery, as mentioned in subsection 2.2. The other two thermal sensors were placed on the ADCS board and were the closest to a solar panel. The power generated by the energy harvesting subsystem at a given time was measured by the SCM.

As shown in Figure 3, there was an inverse correlation between the output power of the solar chargers

Table 2. Power Budget: Heater OFF (OP-MODE 1)/ Heater ON (OP-MODE 2) excluding Payload operation

Component	Power (mW)	Duty Cycle	Avg. power (mW)	+10% margin	Total power (mW)
OBC	264	100%	264.00	26.40	290.40
EPS µC & sensors	20	100%	20.00	2.00	22.00
Battery Heater	908	0% / **33.33%**	0.0 / **302.64**	0.0 / **30.26**	0.0 / **332.90**
AX100 – RX Mode	231	96.40%	222.68	22.27	244.95
AX100 – TX Mode	2640	3.60%	95.04	9.05	104.54
ADCS µC & sensors	66	2.50%	1.65	0.16	1.81
Total power consumption per orbit (mW)					663.70 / **996.60**

and the satellite's temperature. The satellite experienced two high beta angle seasons (marked as A and B in Figure 3) during which the satellite's internal temperature temporarily reached 25-35°C due to increased Sun exposure. Increased exposure to the Sun translated into a decrease in generated power on both occasions. This was an expected result because the efficiency of photovoltaic cells naturally decreases when their surface temperature increases (Maka and O'Donovan, 2021). Figure 3 also shows that the power generated by the energy harvesting subsystem tended to be below the theoretical value of 2.37 W estimated during ground tests. As previously mentioned, the solar chargers implemented a CCCV algorithm to preserve battery health which reduced the chargers' output power at times when the battery reached its full-charge voltage. The received telemetry indicated that the chargers were operating in Constant-Voltage mode for most of the mission, ergo the decrease in generated power.

Nonetheless, there were five instances (marked with the numbers '1' through '5' and arrows in Figure 3) where the battery was discharged by more than 80% due to transceiver TX hang failures (subsection 3.5). Power spikes were observed right after each deep discharge event, evidencing that the energy harvesting subsystem was able to increase its power generation according to the satellite's demand. Three of the five deep discharges (numbered 2, 3, and 4 in Figure 3) took place during the first high beta angle season. Due to decreased solar panel efficiency at the time, the resulting power spikes after failures '2' through '4' were smaller compared to the power spikes after failures '1' and '5'. Finally, the section with no data (marked as C in Figure 3) corresponds to a period when transmissions from the satellite momentarily stopped due to an I2C bus malfunction (further detailed in Chung et al., (2023).

3.1.2. Power Generation Depending on Satellite's Power Demand

It was observed that the power generated by the solar chargers also varied according to the power demanded by the satellite at a given time. The output pins of the solar chargers were directly connected to the central unregulated power line of the satellite; therefore, any bus voltage drop that occurred when the satellite increased its current demand was interpreted as a lower battery voltage by the CCCV algorithm, which then drove the chargers to increase the power flow from the panels to the main bus. For example, at times when the heater turned on, it demanded 0.9 W on the load side of the 3.3 V regulator, which translated into 1 W on the main bus side. This consumption increase caused the main bus voltage to drop by 0.10 V, which triggered an increase in power generated by the chargers. The solar chargers acted as gatekeepers that

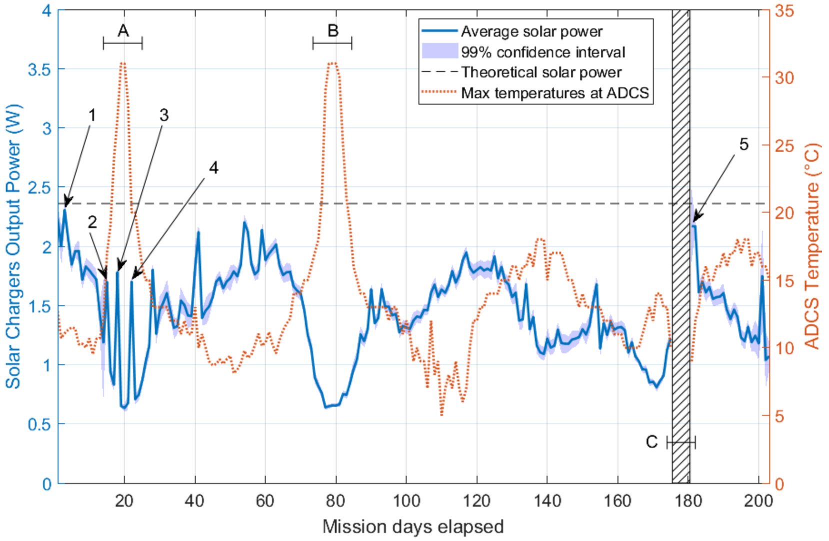

Figure 3. Average power generated by the solar chargers vs. internal temperatures (battery depletion instances marked by numbered arrows; high beta angle seasons marked by letters A & B; I2C bus failure, marked by letter C).

regulated their output power according to the satellite's power demand ensuring that the battery would only have to provide energy to the load in cases when the chargers were not able to supply all the required power at their maximum capacity.

3.1.3. Power Generated per Orbit

Table 3 shows the power generated by the energy harvesting subsystem per orbit. The presented calculations considered the different power generation scenarios that could arise depending on the satellite's power demand (e.g., heater ON/OFF) and on the beta angle conditions. The results correspond to the power generated when the solar chargers were operating in Constant-Voltage mode.

The heater was the main variant considered when classifying the generated power according to the satellite's power demand as the heater typically activated six to eight minutes before the satellite exited Earth's shadow, and it operated for approximately 30 minutes in total during each orbit. This led the heater to be active for approximately 23 minutes under sunlight conditions (equal to a 24.67% orbital duty cycle). It is worth noting that this was the heater's behavior when the eclipse periods per orbit lasted between 30 to 36 minutes. The solar chargers generated 1.97 ± 0.01 W on average at times when the satellite was in sunlight and the heater was active. On the other hand, they generated 1.31 ± 0.01 W on average when the satellite was in sunlight and the heater was inactive. The resulting generated power per orbit when combining all these scenarios was 971 mW.

Table 3 also shows the generated power during high beta angle seasons. The heater did not operate during those times, and the average power generated by the solar chargers decreased to 0.73 ± 0.01 W because the battery remained at full charge and the panels' superficial temperature increased. It should be noted that all these power rates changed when the battery was recharging after depletion events as the solar chargers switched to Constant-Current mode and the energy harvesting subsystem was able to produce 2.14 ± 0.05 W in sunlight, which corresponded to a 1.32 ± 0.03 W orbital average (61.67% duty cycle).

3.1.4. Solar Chargers' Voltage Regulation

As mentioned in subsection 2.1, the solar chargers were used to boost the solar panels' voltage (2.35 V) to the battery's charging voltage (4.20 V). The output voltages of the chargers were configured to this value following the manufacturer's specifications (Microelectronics, 2011). However, telemetry received throughout the mission showed that the battery was being charged at voltages between 4.20-4.27 V which were considerably higher compared to ground test values. Upon inspection of the chargers' design, it was noted that two resistors used on the output voltage dividers of the chargers had different tolerance values (R1 = 1.2MΩ (5% tolerance) and R2 = 510kΩ (1% tolerance)) (see Figure B3). It is hence believed that the tolerance differences caused the resistance ratio to not remain constant when thermal conditions changed the resistors' nominal value, which may have caused the charging voltage of the battery to increase. The recommended charging voltage for Li-ion cells is between 4.15-4.20 V; however, the higher charging voltage did not cause a noticeable impact on the battery's state of health, according to received telemetry. This charging voltage phenomenon was not observed during thermal-vacuum testing on the ground because the battery was not recharged through the solar chargers during the tests.

3.2. Energy Storage

3.2.1. Battery State of Charge

As mentioned in subsection 2.2, the battery gauge had shown to be inaccurate when estimating the parallel Li-ion cells' total charge. Consequently, Eqn.1 was

Table 3**.** Generated Power per Orbit (**Normal** / High Beta) with the Solar Chargers Operating in Constant-Voltage Mode

Scenario	Instant Power (W)	Duty Cycle (%)	Orbit Power (W)
Sunlight & Heater ON	**1.97** / 0.00	**24.67%** / 0.0%	**0.486** / 0.000
Sunlight & Heater OFF	**1.31** / 0.73	**37.00%** / 100%	**0.485** / 0.726
Total power per orbit (W)			**0.971** / 0.726

implemented on the OBC software as a redundancy to approximate the battery’s SOC using the main bus voltage. The equation was designed to translate 4.15 V into 100% charge; however, the telemetry indicated that the main bus voltage was reaching values between 4.20 - 4.27 V on orbit due to the high output voltage of the solar chargers. The original equation implemented on the OBC’s flight software translated these high voltages into SOC values above 100%. Thus, a modified equation based on Eqn. 1 was used to estimate the real SOC of the orbiting satellite through received telemetry. This equation translated a 3.20-4.27 V range into a 0-100% SOC range. The modified equation stands as follows:

$$SOC_{estimate} = 93.458 \cdot Voltage_{MBM} - 299.065 \quad (2)$$

Prior to estimating the battery's SOC on orbit using Eqn. 2, the main bus voltage data was refined by subtracting the voltage drop across the battery’s 150 mΩ internal resistance (see Table C1) caused by the current demanded by the satellite (current values also obtained through telemetry). This was done to obtain a more accurate approximation of the battery's open-circuit voltage, which directly correlated to its SOC. Figure 4 shows the distribution of estimated SOC values, and as observed in the plot, the battery typically remained above 80% of charge throughout most of the mission, evidencing a positive power budget. The only times the battery was below 80% charge was after deployment, because the satellite had spent five months in storage prior to the launch and after transceiver TX hang failures (subsection 3.5), which tended to discharge the battery considerably.

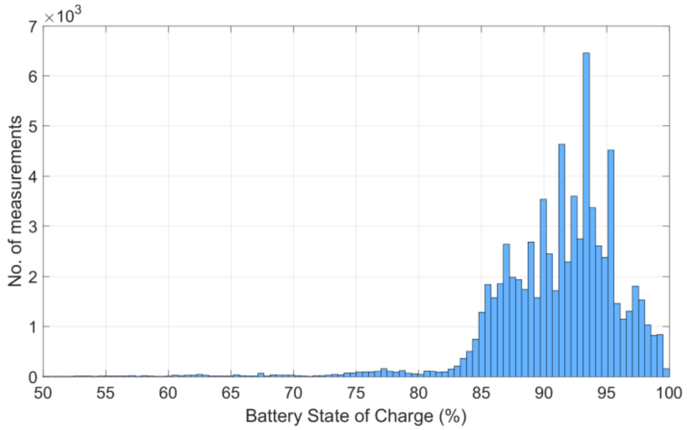

Figure 4. Battery state of charge distribution throughout the mission.

3.2.2. Battery Thermal Regulation

As mentioned in subsection 2.2, the satellite carried a 13-Ω Kapton heater resistor placed between the two stacked Li-ion cells that turned ON when the battery temperature dropped below 3°C and turned OFF when the temperature rose above 5°C. This configuration was set to keep the Li-ion cells from freezing, thus preserving battery health. Figure 5 shows the battery temperature distribution during each week of operations and compares them to the eclipse duration per orbit during each week, indicated by the dotted line. The scale for this dotted line is the same as the temperature scale in the plot but using minutes as units.

Figure 5 shows that the battery temperature typically remained within 1.75°C and 17°C (with 95.5% of samples within this range), which indicated that the heater configuration was adequate to keep the battery from freezing under any orbital condition. There were only two occasions, weeks 17 and 19, during which the battery temperature reached temperatures at or below 0°C with the lowest recorded temperature being -1.25°C. These incidents were the result of two commanded payload operations which required the battery temperature sampling time to be temporarily increased from 30 s to 240 s (Zea et al., 2023). This caused the heater to react slower to temperature drops, allowing the battery temperature to cross the 0°C limit temporarily. These events lasted for about two minutes, with current going into the battery ranging between 50–100 mA. Consequently, these incidents did not have a noticeable effect on the battery's state of health. These incidents proved that the heater operation had been crucial throughout the mission to keep the battery above 0°C, because otherwise the Li-ion cells would have frozen during the first orbits of the mission.

During orbits where the eclipse period reached 36 minutes, the heater would reach an operation time of 30 minutes (31% orbital duty cycle), whereas the heater remained inactive during orbits in the high beta angle seasons. The heater was only operated manually once during the commissioning phase of the mission

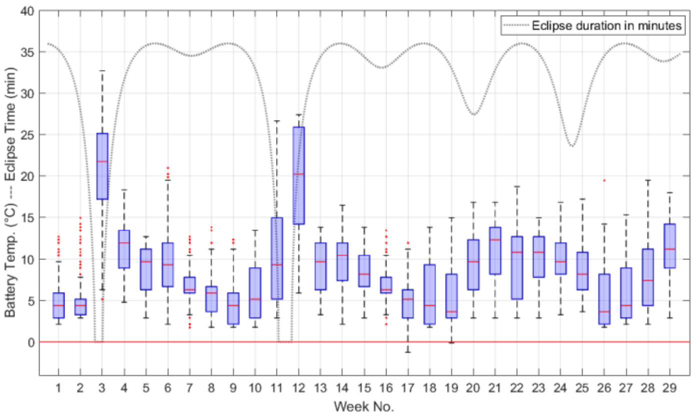

Figure 5. Battery temperature distributions per week compared to eclipse duration.

to test the functionality after launch. In case of a possible thermal sensor failure, the heater emergency mode was configured via ground control station (GCS) commands to periodically activate the heater for 20 minutes and deactivate it for 15 minutes; however, the emergency mode was never activated on orbit. The emergency mode parameters were chosen according to the characteristics of the observed thermal cycles on orbit (see Figure C2). The battery heater and thermal sensor operated nominally during all 3,215 orbits during which the satellite was operational.

The heater correctly activated every time that the battery temperature dipped below 3°C, according to the battery thermal sensor, and deactivated when the temperature increased above 5°C. After heater activation, the temperature typically continued to decrease, albeit at a slower rate, for approximately seven minutes before it started to rise again. The observed delay in temperature increase was most likely the result of the battery taking a while to warm up all the way to the thermal sensor placed on top of the battery stack. This evidenced that the 3°C heater activation threshold was adequately selected when programming the flight software, because a lower threshold would have likely caused the battery sections furthest from the heater to momentarily reach a temperature below 0°C before it started to increase.

3.2.3. Battery Degradation

Throughout the on-orbit mission, telemetry indicated that the battery was performing nominally with no unexpected external resets occurring during eclipse periods, and data measured by the battery gauge and bus monitors showed that the battery power remained stable and adequate for operations until the end of the mission. The state of health data measured by the battery gauge showed no decrease in time; however, it was observed that the measured state of health (SOH) values had a strong dependency on battery temperature. Figure 6 shows the SOH data collected throughout the mission versus battery temperatures. It can be observed that the battery's SOH reached 91%, which was the SOH value acquired during ground tests, at times when the battery temperature reached 25°C (room temperature) on orbit; however, the SOH dropped to values near 75% when the temperature dropped below 5°C. As observed in the plot, the SOH typically varied between 75% and 85% which indicates a battery capacity varying between 3,000 - 3,400 mAh during the mission.

As previously mentioned, the battery suffered five deep discharge cycles (depth of discharge >80%) caused by transceiver TX hang failures throughout the mission, with four of them causing external resets due to battery depletion (more details in subsection 3.5). Other transceiver TX hang failures occasionally caused the SOC to drop below 50%, without causing full battery depletion. The rest of the time, the battery was cycled with shallow depths of discharge (5% - 20%). This, combined with the solar chargers' CCCV algorithm, helped preserve the battery SOH.

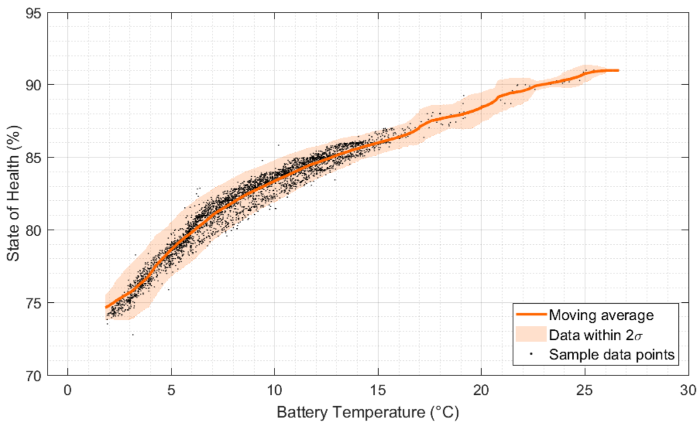

Figure 6. Battery temperature distributions per week compared to eclipse duration.

3.3. Power Distribution & Protection

3.3.1. Heater Performance

As mentioned in subsection 3.2, the battery heater operated as intended and kept the battery from freezing, demanding an average current of 272.28 ± 0.02 mA, which corresponded to 898.52 ± 0.07 mW at 3.3 V. This power consumption indicated nominal operation according to the power budget (Table 2). Furthermore, the heater FPB did not detect any overcurrent or short-circuit condition that would have indicated a heater failure.

3.3.2. ADCS and Payload Performance

By design, the ADCS system was in low power mode at times when the EPS system polled its power monitors; thus, the EPS sensors always detected a current consumption of 0 mA from ADCS. The ADCS system's performance on orbit was nominal, as detailed in (Alvarez et al., 2023), evidencing nominal power supply to the system via the 3.3 V and 5.0 V buses, and correct switching and protection by its FPB.

The Payload system was only occasionally activated when the satellite performed an OBC watchdog reset (and the piezoelectric motor rotated the payload's carousel), and when commands were sent from the GCS to perform a payload operation. The payload camera and motor operated as intended, as evidenced by the system being able to capture pictures and sending them back to ground, as detailed in (Zea et al., 2023), evidencing nominal power supply via the 3.3 V and 7.6 V buses. The payload board typically demanded 60 mA when the camera was in stand-by, and the camera demanded 195 mA when it was executing a picture capture. These values were nominal for the system. Regarding the motor, its power consumption could not be measured because the current transient was too fast to be detected by the EPS sensors. Furthermore, the payload FPB indicated nominal performance of the complete system on orbit (no overcurrent or short-circuit). The I2C isolators implemented on both systems worked as expected, correctly disconnecting them from the main I2C bus when they were powered off.

3.3.3. OBC and COMMS Performance

The Nanomind A3200 OBC performed as intended throughout the whole mission, evidencing nominal power supply via the 3.3 V bus. The only four external resets that the OBC perceived were caused by battery depletions due to the transceiver TX hang failures. The COMMS system, composed of the Gomspace's Nanocom AX100 transceiver, performed nominally for most of the mission, aside from its TX hang failures (subsection 3.5). It was able to receive the commands sent to the satellite via the GCS and also transmitted the satellite's telemetry, health data, and commanded payload data back to Earth. The AX100 typically consumed a nominal average current of 70.44 mA in RX mode according to the telemetry, which corresponded to an average of 232.45 mW at 3.3 V. This matches the data detailed in Table 2, indicating nominal operation. Consumption during TX mode was not measured because the beacons were sent after the EPS module polled its sensors.

3.4. On-orbit Power Consumption

Table 4 shows the power consumption and duty cycle for each system on orbit with most results matching the power budget detailed in Table 2, evidencing nominal operation in space and accurate pre-flight modeling. The only variation was the duty cycle of the heater on orbit. The maximum duty cycle for the battery heater on orbit was 31% when the satellite was experiencing the maximum eclipse duration of 36 minutes; consequently, the total power consumption per orbit was 969.92 mW instead of the 996.55 mW estimated in Table 2.

As previously detailed in Table 3, the solar chargers generated 971 mW on average per orbit when the solar chargers were operating in Constant-Voltage mode; thus, the resulting power margin between the generated and consumed power (969.92 mW) was only 1.08 mW. This indicates that the system remained close to equilibrium (0 W margin), with the chargers generating just enough power to cover the total energy demanded during sunlight and eclipse periods. The battery guaranteed continuity of operations during the latter. It is important to note that this was the typical

Table 4. On-orbit Power Consumption (**Nominal Ops.** / High beta periods) Excluding Payload Operation

Component	Power (mW)	Duty Cycle	Avg. power	+10% regulator loss	Total power (mW)
OBC	264	100%	264.00	26.40	290.40
EPS μC & sensors	20	100%	20.00	2.00	22.00
Battery Heater	898	**31%** / 0%	**278.38** / 0	**27.08** / 0.0	**306.22** / 0.0
AX100 – RX Mode	231	96.40%	222.68	22.27	244.95
AX100 – TX Mode	2640	3.60%	95.04	9.05	104.54
ADCS μC & sensors	66	2.50%	1.65	0.16	1.81
Total power consumption per orbit (mW)					**969.92** / 663.70

behavior of the system when the eclipse periods lasted more than 30 minutes and the battery was at >80% charge.

As mentioned in subsection 3.1, the solar chargers increased their generated power per orbit to 1.32 W on average when they switched to Constant-Current mode due to perceived low battery voltage after depletion events. This higher power generation increased the power margin to 350 mW, allowing the battery to recharge. It took approximately 30 hours for the solar chargers to recharge the battery from 0% to >80% charge, all while the satellite continued nominal operations. Table 4 also shows that the satellite only demanded 0.66 W per orbit during high beta angle seasons (no eclipse) because the heater remained inactive. The solar chargers produced 0.73 W on average under these same conditions (see Table 3), providing a positive power margin of 70 mW. This last result, along with the others, evidence that the system tended towards equilibrium (battery fully charged) regardless of the operating conditions, including battery depletions and high beta angle seasons, during which the panels' efficiency decreased.

3.5. On-orbit Recorded Glitches and Failures

3.5.1. Transceiver TX Hang Failures

Although the COMMS module performed nominally most of the time, it did present failures on orbit. The module experienced a total of 24 recorded TX hang failures throughout the mission during which the AX100 transceiver continuously transmitted incorrect data frames until the OBC performed a watchdog reset, or the battery completely discharged, causing an external reset on the satellite. Typically, the AX100 continuously consumed 775.76 ± 0.01 mA or 2.56 ± 0.01 W during these failures (constant TX mode consumption). The heater did not operate at those times because the failures caused a +10°C increase in battery temperature due to the continuous current draw. The power consumption per orbit increased from 0.969 W to 3.13 W, while the solar chargers increased their power generation to 1.32 W per orbit. This resulted in a negative power margin of -1.81 W. Due to the negative power margin, the battery completely discharged after approximately six hours at times when the COMMS module entered into an anomalous mode. For this reason, the OBC watchdog timer cycle was changed via GCS command from 24 to 2 hours to prevent the failures from causing full battery depletions and preserve battery health.

Five of the 24 failures (marked by numbers 1-5 in Figure 3) discharged the battery by more than 80%, with four of them causing external resets. The fourth external reset (marked by number 5 in Figure 3) was intentionally performed by temporarily reverting the watchdog timer cycle to 24 hours and waiting for a transceiver TX hang failure to occur and deplete the battery. The failure was used to cause an external reset to recover the satellite from an I2C bus hang, which is further detailed in Chung et al. (2023). The 24th failure happened during a second I2C bus hang experienced by the satellite, which had left the Payload system energized and the battery without its heater for 52 orbits. The watchdog timer cycle had also been reverted to 24 hours to allow another external reset via a TX hang failure to occur. This time, however, the satellite did not communicate again with the GCS after the 24th TX hang failure depleted the battery, marking the end of its life. It is believed that the Li-ion cells degraded by the freezing temperatures, and the atypically high current pull of the last TX hang failure caused a catastrophic battery failure. The causes for the TX hang failures are yet to be determined.

3.5.2. AX100 RX Current Increase

Another atypical AX100 behavior was observed thrice during the mission. On three occasions, the AX100 unexpectedly raised its RX average current consumption by 20 mA, from 70.44 mA to 90.44 mA with no other indicators of atypical operation besides the increased current. Contrary to the TX hang failures, this glitch persisted after the execution of OBC watchdog resets. The only way to solve this issue was through the execution of COMMS hardware resets via GCS commands. After the resets, the power consumption returned to nominal values. The causes for this glitch are also yet to be determined.

3.5.3. Battery Gauge Failures

During the last ground tests performed prior to satellite delivery, the battery gauge sensor was accidentally subjected to high temperatures. The EPS circuit board had just been coated with a urethane insulator (Huntsman, Cat. No. Arathane 5753-A/B) to protect the components from the harsh space environment. During EPS board testing, it was observed that the battery gauge was heating up and causing the board to shut down. The insulation was removed from around the sensor and the high temperatures could not be replicated. Due to time constraints, the battery gauge was not replaced because it was observed that it still performed its basic measurements correctly.

However, after the incident and during space operations, it was observed that the sensor would occasionally return incorrect all-zero data when the current flowing into or from the battery surpassed approximately 400 mA. The frequency of these glitches also increased during high beta angle seasons when the internal temperature of the satellite increased. Thus, it is hypothesized that increase in sensor temperature due to high current demands and high beta angle seasons was the reason behind the glitches. Telemetry packets which presented incorrect data from the battery gauge amounted to 8.62% of the total number of packets received during the mission.

4. Conclusions

To summarize, the power generation carried out by the energy harvesting subsystem on Quetzal-1 depended on three main factors: the panels' surface temperature, the battery's state of charge, and the satellite's power demand. In terms of panel temperature, the satellite experienced two high beta angle seasons with no eclipse during which the power generation decreased due to the reduced panels' efficiency caused by the increase in their temperature. For battery state of charge, the telemetry indicated that the battery remained above 80% of charge throughout most of the mission, and the solar chargers mostly operated in Constant-Voltage mode reducing the generated power to avoid overcharging the battery. Finally, for power demand, increases in satellite power demand translated into main bus voltage drops that caused the solar chargers to generate more power. The solar chargers acted as gatekeepers, generating enough power to meet the satellite's demand without overcharging the battery. This ensured that the battery only supplied power if the chargers could not meet the full power demand (e.g., during eclipse or peak power demand).

The energy harvesting subsystem generated 971 mW per orbit when the chargers were operating in Constant-Voltage mode and the satellite consumed 969.92 mW when the eclipse periods lasted more than 30 minutes. Thus, under these conditions, the system remained in equilibrium with a positive power margin of 1.08 mW. Under high beta angle conditions, the power generation and demand decreased to 726 mW and 663.70 mW, respectively; thus, the satellite had a positive power margin of 62.3 mW. Finally, when the solar chargers were operating in Constant-Current mode, the energy harvesting subsystem generated 1.32 W, increasing the power margin to 350 mW. This allowed the battery to recharge from 0% to >80% in approximately 30 hours. As evidenced, the EPS ensured a positive power budget regardless of the operating conditions.

The battery heater configuration proved adequate to maintain the battery above 0°C regardless of the duration of the eclipse periods, which could reach a maximum of 36 minutes. The battery, the heater, and the battery thermal sensor all operated nominally throughout the satellite's life. The battery system provided a stable power source during eclipse periods where no unexpected external resets were detected. The battery's state of health varied between 75% and 85% due to temperature fluctuations, which translates into 3,000 - 3,400 mAh capacity during the mission. Two I2C bus failures left the satellite without heater operation for a combined total of nine days; thus, battery freezing is hypothesized to be the contributor to the satellite's end of life.

The transceiver TX hang failures where the AX100 operated in constant TX mode increased the satellite's power demand to 3.13 W and caused the solar chargers to increase their power generation to 1.32 W per orbit. This resulted in a negative power margin of -1.81 W, which led to full battery depletion in approximately six hours. This problem was tackled by reducing the watchdog timer reset period to two hours, which fixed the issue quickly enough to avoid external resets due to full battery depletion.

5. Recommendations

The authors recommend the use of individual thermal and power sensors for each solar panel to monitor their performance more accurately. When selecting resistors for voltage dividers used to calibrate regulators or solar chargers, it is recommended to choose resistors with equal tolerance value to avoid changes in resistor ratio due to thermal fluctuations in space. It is also recommended to add dissipation circuitry to the battery to prevent the charging voltage from exceeding the values recommended by cells' manufacturers. Furthermore, it is recommended to implement battery gauge sensors with the capability of monitoring two parallel battery cells individually to obtain more accurate state of charge and state of health measurements. Additionally, it is recommended to add autonomy to the EPS flight software so that the µC can unilaterally decide to activate or deactivate the battery heater in case communication with OBC is temporarily lost, as in the case of this mission. Finally, the authors recommend implementing redundancy to communication buses (e.g., I2C lines) or bus resetting capabilities to avoid single-point system failures.

Acknowledgments

The authors thank Universidad del Valle de Guatemala for its support, which made this project possible. CubeSat safety reviews, and launch and deployment from the International Space Station were provided under KiboCUBE, a joint program of the United Nations Office for Outer Space Affairs (UNOOSA) and Japan Aerospace Exploration Agency (JAXA). Environmental testing was done thanks to the support of the United Kingdom Space Agency (UKSA) and ASTROSAT. The authors also acknowledge and thank Dr. Scott Palo and Dr. Andrew Dahir for the invaluable support they provided to the Quetzal-1 project. Dr. Dahir is also thanked for reviewing this manuscript. The authors would also like to thank Mr. Kendy Cipriano for his incredible work soldering the electronic components on the Quetzal-1's circuit boards, and Mrs. Estela Morales for supporting the project's administrative activities. Finally, the authors would like to thank all the students, professors, advisors, and organizations that contributed to the design and development of Quetzal-1's EPS and other systems.

References

Alvarez, D. et al. (2023): On-Orbit Performance of a Passive Attitude Control System, *J. of Small Satellites (JoSS)*, Vol. 12 (2), p. 1231. Available at: www.jossonline.com.

Arnold, S. et al. (2012): QbX-The CubeSat Experiment, in *Proc. 26th Ann. AIAA/USU Conf. on Small.Satellites*, Logan, UT. Available at: https://digitalcommons.usu.edu/cgi/viewcontent.cgi?article=5591090&context=smallsat (accessed Apr. 20, 2021).

ASTM (2014): Standard Solar Constant and Zero Air Mass Solar Spectral Irradiance Tables (E490-

00a). Available at: http://materialstandard.com/wp-content/uploads/2019/10/E490-00a-Reapproved-2014.pdf (accessed Apr. 27, 2021).

AzurSpace (2016): 30% Triple Junction GaAs Solar Cell Assembly - Type: TJ Solar Cell Assembly 3G30A - Improved Voltage at Maximum Power Point, Available at: http://www.azurspace.com/images/products/0003401-01-01_DB_3G30A.pdf (accessed Nov. 21, 2020).

Birnie, J. et al. (2023): Novel Approach for Structural Finite Element Analysis on CubeSat's Bolted Connections. [Unpublished manuscript.]

Chung, K. et al. (2023): Design, Development, and Pre-Flight Testing of the Fault-Tolerant Command and Data Handling Subsystem of the Quetzal-1 Nanosatellite. [Unpublished manuscript.]

DataPower (2018): Polymer Li-Ion Rechargeable Battery - DTP605068. Available at: https://www.marutsu.co.jp/contents/shop/marutsu/datasheet/836419.pdf, (accessed Nov. 21, 2020).

JAXA (2018): JX-ESPC-101132-CJEM Payload Accommodation Handbook. Available at: https://www.unoosa.org/documents/pdf/psa/hsti/KiboCUBE/JEM_Payload_Accommodation_Handbook.pdf (accessed Feb. 25, 2021).

Li, X., Palo, S., Kohnert, R. et al. (2012): Colorado Student Space Weather Experiment: Differential Flux Measurements of Energetic Particles in a Highly Inclined Low Earth Orbit, Dynamics of the Earth's Radiation Belts and Inner Magnetosphere, *Geophys. Monogr. Ser.*, Vol. 199, pp. 385–404. doi: 10.1029/2012GM001313.

Maka, A. and O'Donovan, T. (2021): Effect of Thermal Load on Performance Parameters of Solar Concentrating Photovoltaic: High-efficiency Solar Cells, *J. of Energy and Built Environment*, Vol. 3, Southwest Jiatong University, China. pp. 201–209. doi: 10.1016/j.enbenv.2021.01.004.

Martínez, M. et al. (2018): Guatemala's Remote Sensing CubeSat - Tools and Approaches to Increase the Probability of Mission Success, in *Proc. 32nd Ann. AIAA/USU Conf. on Small Satellites*, Logan, UT. Available at: https://digitalcommons.usu.edu/cgi/viewcontent.cgi?article=4288&context=smallsat (accessed Apr. 25, 2021).

Microchip (2014): Low-Noise, Positive-Regulated Charge Pump. Available at: https://ww1.microchip.com/downloads/en/DeviceDoc/20001752C.pdf (accessed Nov. 21, 2020).

Microelectronics (2011): High Efficiency Solar Battery Charger with Embedded MPPT. Available at: https://www.st.com/resource/en/datasheet/spv1040.pdf (accessed Nov. 21, 2020).

NASA (2017): Crewed Space Vehicle Battery Safety Requirements. Available at: https://standards.nasa.gov/standard/jsc/jsc-20793 (accessed Feb. 25, 2021).

Oltrogge, D. and Leveque, K. (2011): An Evaluation of CubeSat Orbital Decay, in *Proc. 25th Ann AIAA/USU Conf. on Small Satellites*, Logan, UT. Available at: https://digitalcommons.usu.edu/cgi/viewcontent.cgi?article=4288&context=smallsat (accessed Mar. 13, 2021).

Pajusalu, M. et al. (2012): Design of the Electrical Power System for the ESTCube-1 Satellite, *Latvian J. of Physics and Technical Sciences*, Vol. 49(3), pp. 16–24. doi: 10.2478/v10047-012-0014-4.

Petzl, M., Kasper, M., and Danzer, M.A. (2015): Lithium Plating in a Commercial Lithium-Ion Battery--A Low Temperature Aging Study, *J. of Power Sources*, Vol. 275, pp. 799–807. doi: 10.1016/j.jpowsour.2014.11.065.

Quetzal-1 Team (2021): Quetzal-1's Open-Source Flight Software. Available at: https://github.com/Quetzal-1-CubeSat-Team (accessed May 01, 2021).

Sumanth, R. (2019): Computation of Eclipse Time for Low-Earth Orbiting Small Satellites, *Int. J. of Aviation, Aeronautics, and Aerospace*, Vol. 6(5), p. 15. doi: 10.15394/ijaaa.2019.1412.

Taniguchi, F., Akagi, H., and Matsumoto, K. (2020): KiboCUBE - UNOOSA/JAXA Cooperation Program for Capacity Building by Using the Innovative CubeSat Launch Opportunity from ISS Kibo, Space Capacity Building in the XXI Century, Vol. 22, pp. 85–94. doi: 10.1007/978-3-030-21938-3_8.

Texas Instruments (2013): System-Side Impedance Track Fuel Gauge. Available at: https://www.ti.com/product/BQ27441-G1 (accessed Nov. 21, 2020).

Texas Instruments (2016a): TPS61089x 12.6-V, 7-A Fully Integrated Synchronous Boost Converters in 2.0-Mm X 2.5-Mm VQFN Package. Available at: https://www.ti.com/product/TPS61089 (accessed Nov. 21, 2020).

Texas Instruments (2016b): TPS63070 2-V to 16-V Buck-Boost Converter With 3.6-A Switch Current. Available at: https://www.ti.com/product/TPS63070 (accessed Nov. 21, 2020).

Zea, L. et al. (2016): A Methodology for CubeSat Mission Selection. *J. of Small Satellites (JoSS)*, Vol.5(3), pp. 483–511. Available at: https://jossonline.com/page_id1897 (accessed Feb. 15, 2021).

Zea, L. et al. (2023): Academic Development and Space Operations of a Multispectral Imaging Payload for 1U CubeSats. [Unpublished manuscript.]

Appendix A. Quetzal-1 Assembly Images

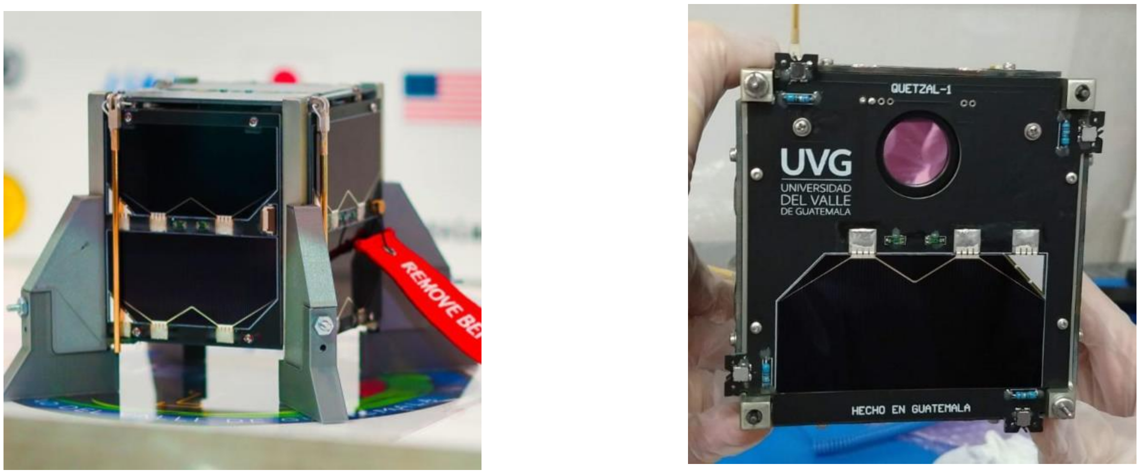
REMOVE BE
QUETZAL-1
UVG
UNIVERSIDAD
DEL VALLE
DE GUATEMALA
HECHO EN GUATEMALA

Figure A1. Left: Solar panels with two photovoltaic cells covering the -X, +Y, and +Z faces of Quetzal-1. Right: A solar panel with camera boresight and one photovoltaic cell covering the -Z face of the satellite.

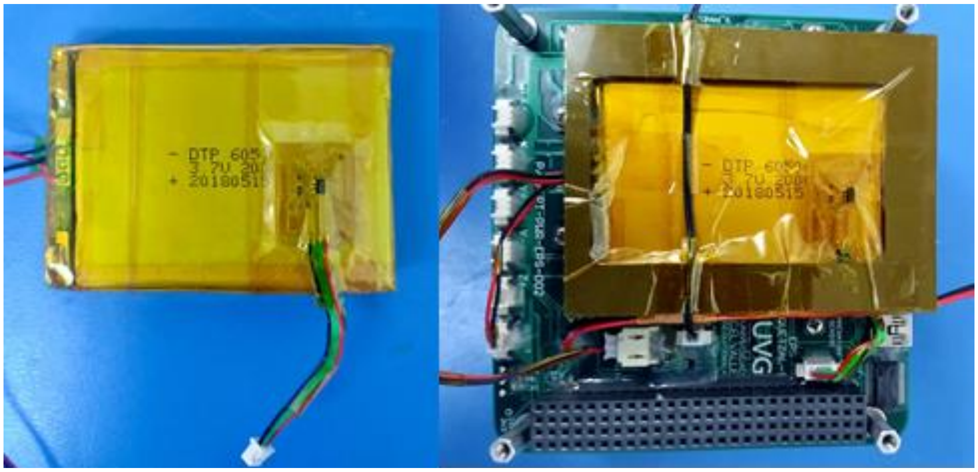

Figure A2: Stacked battery cells wrapped in Kapton tape, with heater in between and thermal sensor fixed to the top of the battery stack with the Kapton tape to maintain contact (Left: standalone battery stack; Right: Battery assembled into EPS).

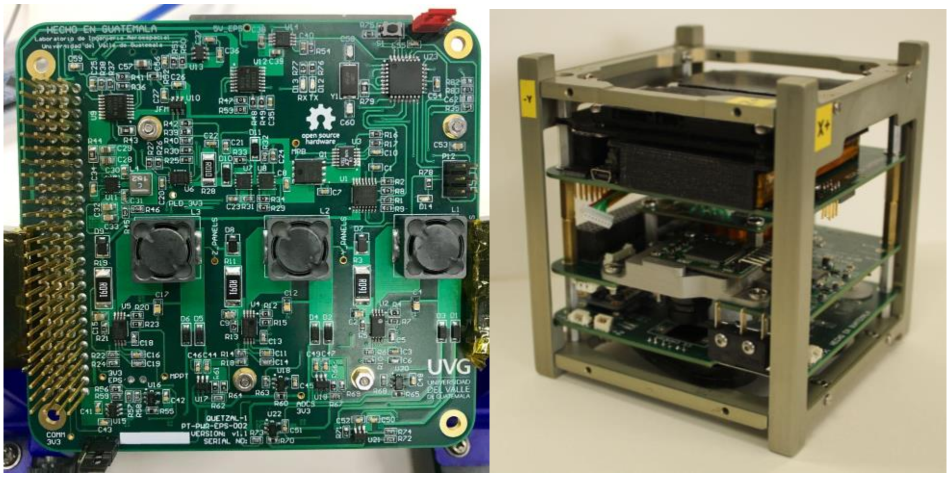
HECHO EN GUATEMALA
UVG
-Y
X+

Figure A3: Left: Populated EPS circuit board of Quetzal-1 -- Right: Quetzal-1 boards stacked (EPS is third board from bottom to top).

Appendix B. EPS Circuit Schematics

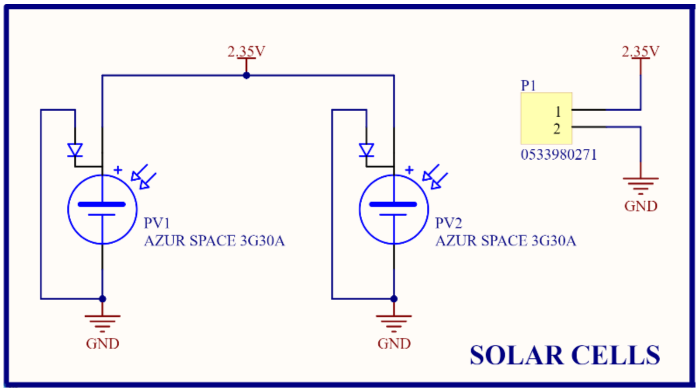
2.35V
2.35V
P1
1
2
0533980271
GND
PV1
AZUR SPACE 3G30A
PV2
AZUR SPACE 3G30A
GND
GND
SOLAR CELLS

Figure Figure B1. Circuit schematic of a single solar panel with two AzurSpace 3G30A cells in parallel.

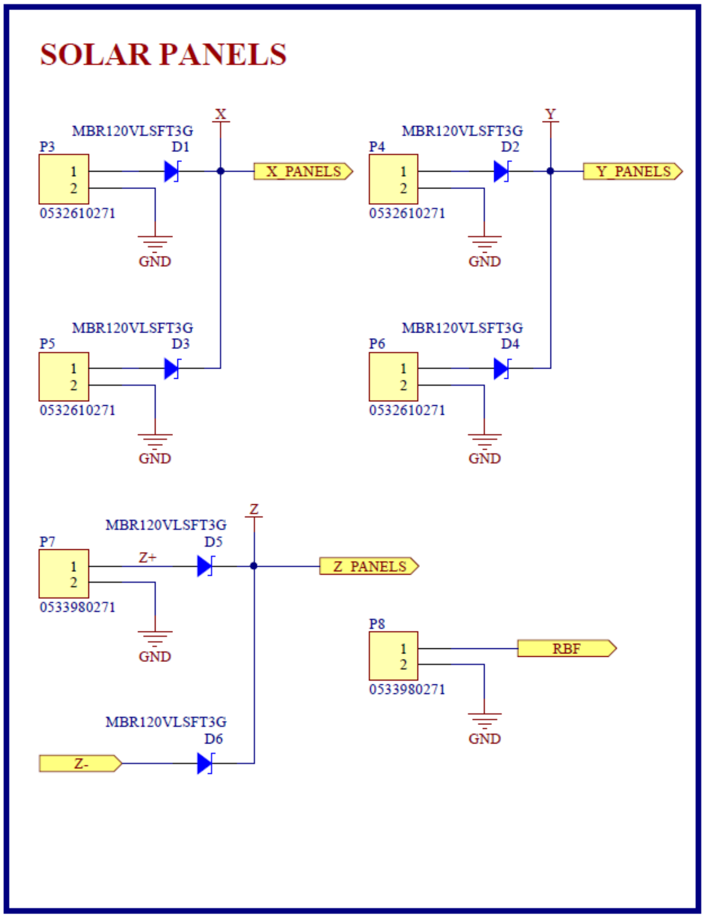
SOLAR PANELS
MBR120VLSFT3G
P3
D1
X
X_PANELS
0532610271
GND
MBR120VLSFT3G
P4
D2
Y
Y_PANELS
0532610271
GND
MBR120VLSFT3G
P5
D3
0532610271
GND
MBR120VLSFT3G
P6
D4
0532610271
GND
MBR120VLSFT3G
P7
D5
Z+
Z
Z_PANELS
0533980271
GND
P8
RBF
0533980271
GND
MBR120VLSFT3G
D6
Z-

Figure B2. Circuit schematic of the solar panels paired in parallel configurations, with ideal blocking diodes at the panels' outputs.

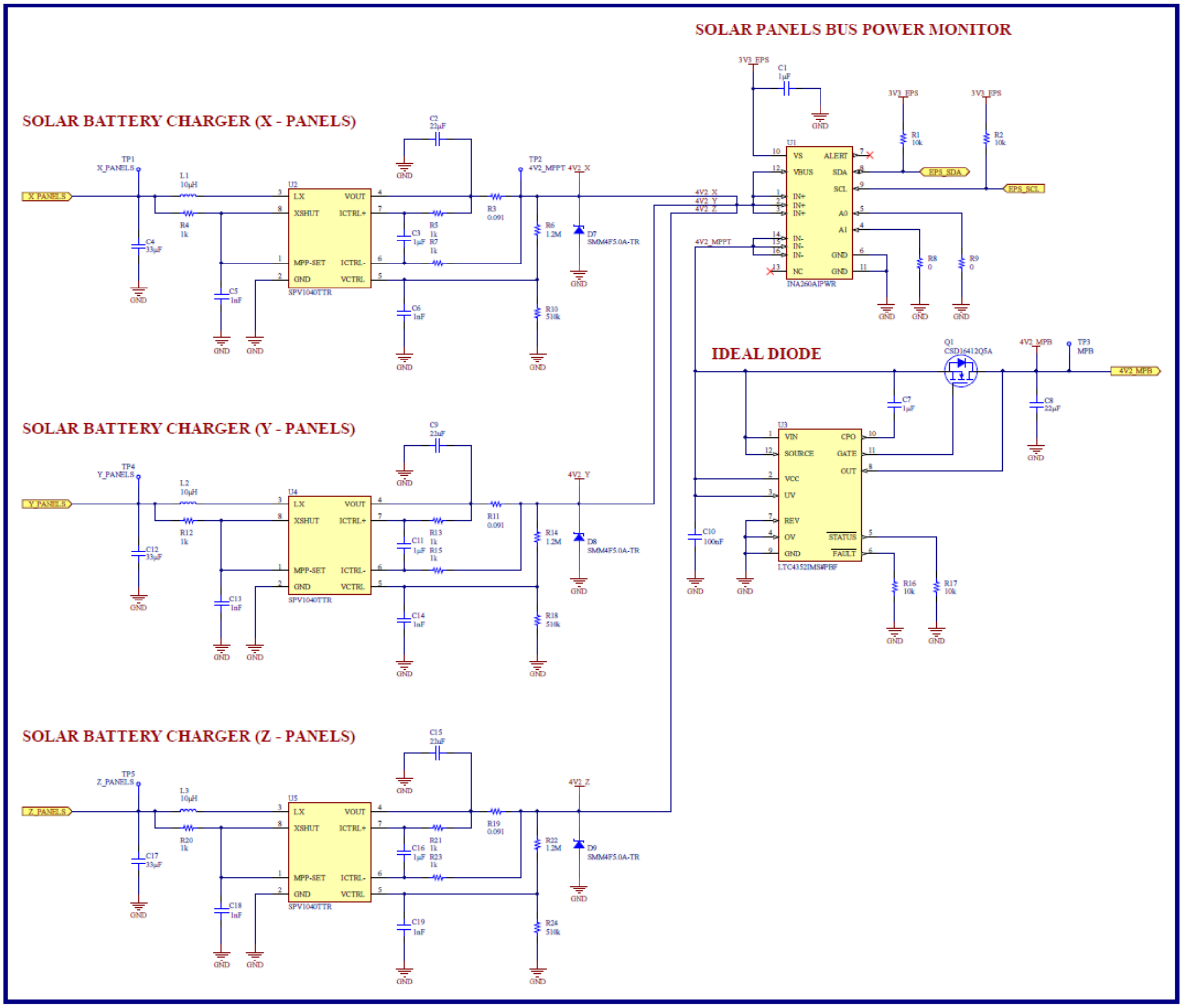
SOLAR PANELS BUS POWER MONITOR
SOLAR BATTERY CHARGER (X - PANELS)
SOLAR BATTERY CHARGER (Y - PANELS)
SOLAR BATTERY CHARGER (Z - PANELS)
IDEAL DIODE
X_PANELS
Y_PANELS
Z_PANELS
SPV1040TTR
INA260AIPWR
LTC4352IMS#PBF
CSD16412Q5A
SMM4F5.0A-TR
EPS_SDA
EPS_SCL
4V2_MPB
4V2_X
4V2_Y
4V2_Z
4V2_MPPT
3V3_EPS
GND

Figure B3. Circuit schematic of the three solar chargers on board, the Solar Channel Monitor (SCM), and the general ideal blocking diode implemented to prevent reverse quiescent currents from the battery to the energy harvesting subsystem.

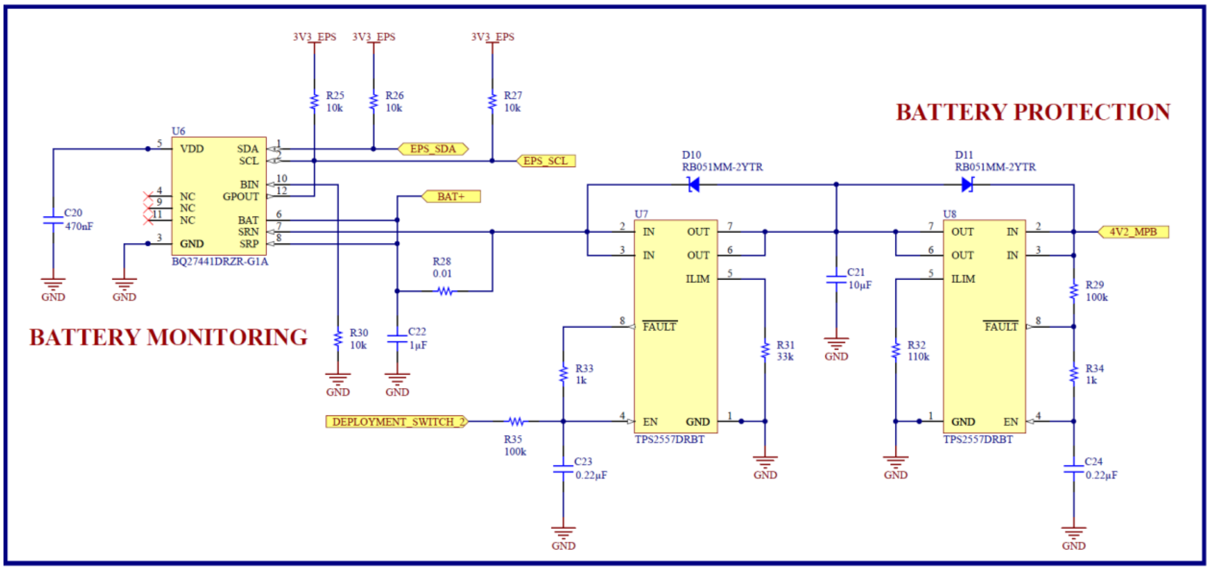
BATTERY PROTECTION
BATTERY MONITORING
3V3_EPS
R25 10k
R26 10k
R27 10k
U6
VDD
SDA
SCL
BIN
GPOUT
NC
BAT
SRN
SRP
GND
BQ27441DRZR-G1A
C20 470nF
EPS_SDA
EPS_SCL
BAT+
R28 0.01
R30 10k
C22 1µF
D10 RB051MM-2YTR
D11 RB051MM-2YTR
U7
U8
IN
OUT
ILIM
FAULT
EN
GND
TPS2557DRBT
C21 10µF
R31 33k
R32 110k
R29 100k
R33 1k
R34 1k
R35 100k
C23 0.22µF
C24 0.22µF
4V2_MPB
DEPLOYMENT_SWITCH_2
GND

Figure B4. Schematic of the battery protection [NOTE: R40 is 15 kΩ, R45 is 470 kΩ, and R46 is 150 kΩ].

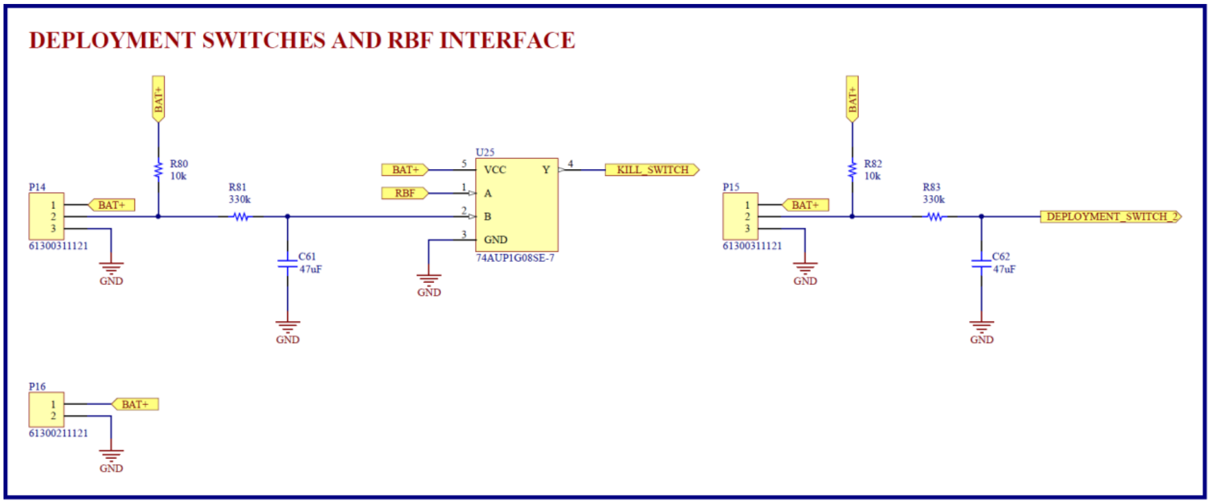
DEPLOYMENT SWITCHES AND RBF INTERFACE
BAT+
R80
10k
P14
1
2
3
BAT+
61300311121
GND
R81
330k
C61
47uF
GND
U25
BAT+
RBF
5
1
2
3
VCC
A
B
GND
Y
4
KILL_SWITCH
74AUP1G08SE-7
GND
BAT+
R82
10k
P15
BAT+
61300311121
GND
R83
330k
DEPLOYMENT_SWITCH_2
C62
47uF
GND
P16
1
2
BAT+
61300211121
GND

Figure B5**.** Circuit schematic of the deployment switches and Remove Before Flight (RBF) switch system (kill switch).

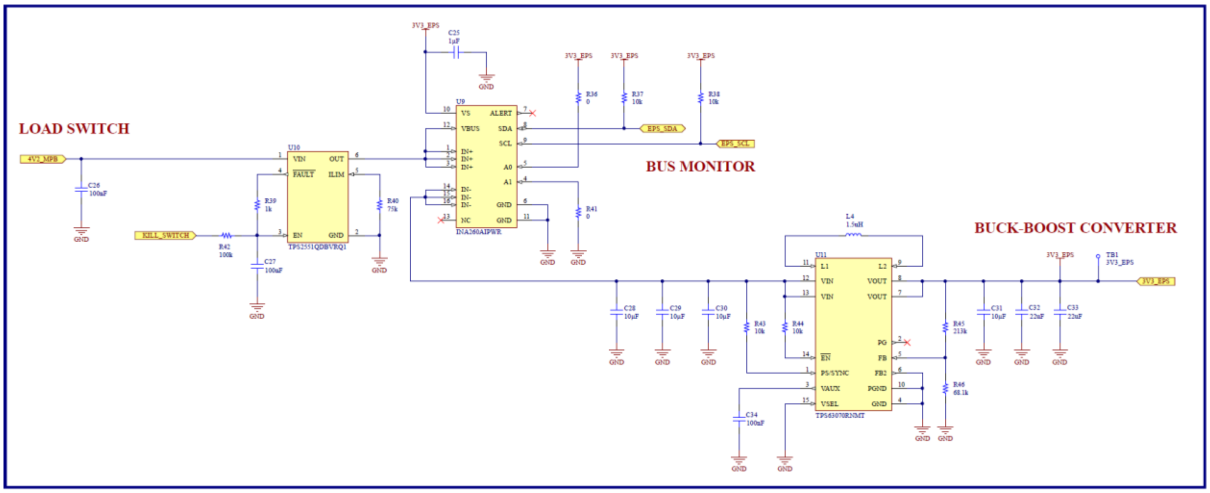
LOAD SWITCH
4V2_MPB
C26
100nF
GND
U10
VIN
FAULT
EN
OUT
ILIM
GND
TPS2551QDBVRQ1
R39
1k
R40
75k
KILL_SWITCH
R42
100k
C27
100nF
GND
3V3_EPS
C25
1µF
GND
U9
VS
VBUS
IN+
IN-
NC
ALERT
SDA
SCL
A0
A1
GND
INA260AIPWR
3V3_EPS
R36
0
R37
10k
R38
10k
EPS_SDA
EPS_SCL
R41
0
BUS MONITOR
BUCK-BOOST CONVERTER
L4
1.5uH
U11
L1
VIN
EN
PS/SYNC
VAUX
VSEL
L2
VOUT
PG
FB
FB2
PGND
GND
TPS63070RNMT
C28
10µF
C29
10µF
C30
10µF
R43
10k
R44
10k
C34
100nF
R45
213k
R46
68.1k
C31
10µF
C32
22uF
C33
22uF
3V3_EPS
TB1
3V3_EPS
3V3_EPS
GND

Figure B6. Circuit schematic of the 3.3 V regulator, with its load switch connected to the kill switch (see Figure B5) and Main Bus Monitor (MBM).

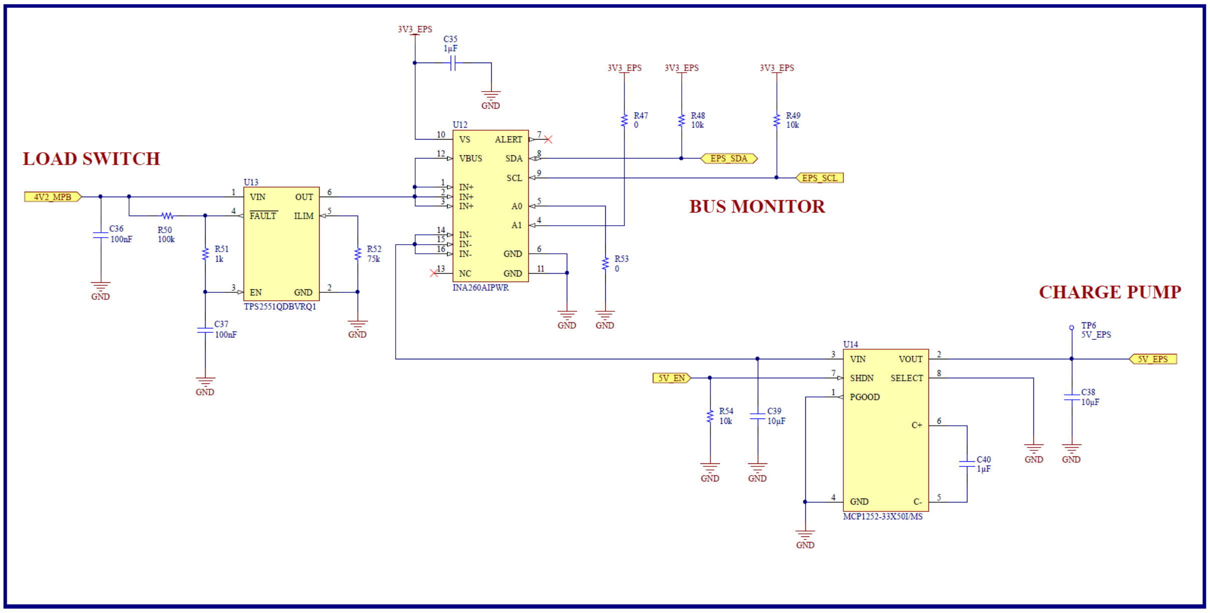
LOAD SWITCH
BUS MONITOR
CHARGE PUMP
4V2_MPB
C36
100nF
R50
100k
R51
1k
C37
100nF
U13
VIN
FAULT
EN
OUT
ILIM
GND
TPS2551QDBVRQ1
R52
75k
3V3_EPS
C35
1μF
U12
VS
VBUS
IN+
IN-
NC
ALERT
SDA
SCL
A0
A1
GND
INA260AIPWR
R47
0
R48
10k
R49
10k
R53
0
EPS_SDA
EPS_SCL
U14
VIN
SHDN
PGOOD
GND
VOUT
SELECT
C+
C-
MCP1252-33X50I/MS
5V_EN
R54
10k
C39
10μF
C40
1μF
C38
10μF
TP6
5V_EPS
5V_EPS
GND

Figure B7. Circuit schematic of 5 V regulator, with load switch and Secondary Bus Monitor (SBM) [NOTE: R52 is 15 kΩ].

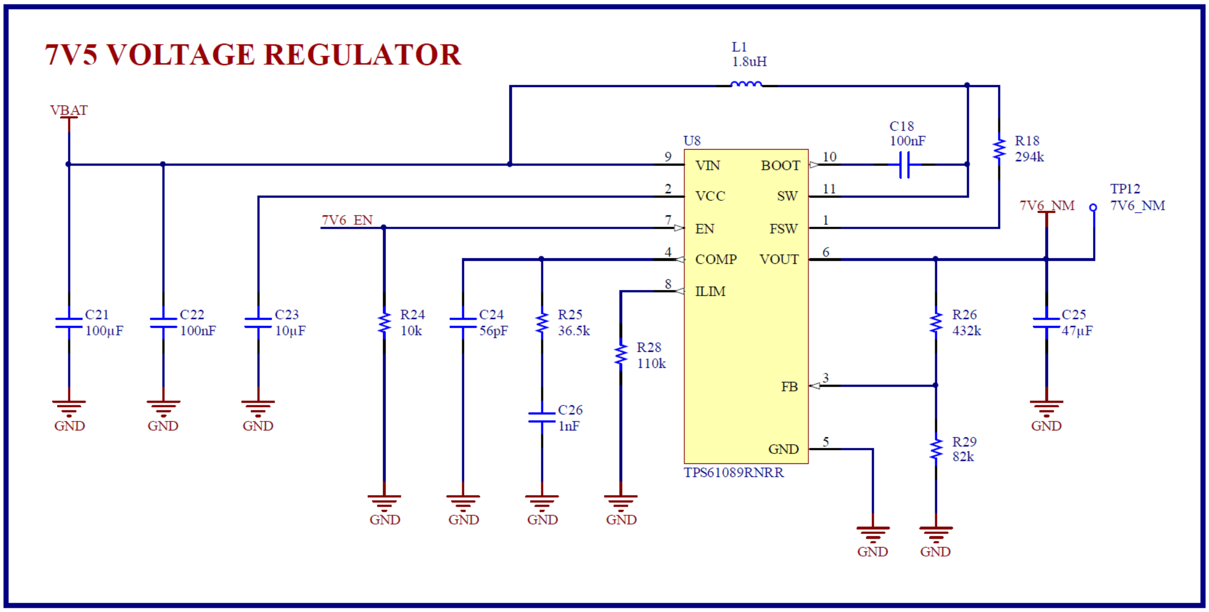
7V5 VOLTAGE REGULATOR
L1
1.8uH
VBAT
U8
VIN
VCC
EN
COMP
ILIM
BOOT
SW
FSW
VOUT
FB
GND
TPS61089RNRR
C18
100nF
R18
294k
TP12
7V6_NM
7V6_NM
7V6_EN
C21
100μF
C22
100nF
C23
10μF
R24
10k
C24
56pF
R25
36.5k
C26
1nF
R28
110k
R26
432k
R29
82k
C25
47μF
GND

Figure B8. Circuit schematic of the 7.6 V regulator placed on the Payload system’s circuit board [NOTE: Even though the schematic is titled 7V5 Voltage Regulator, the true output voltage of the regulator with the configuration shown in the picture is 7.6 V].

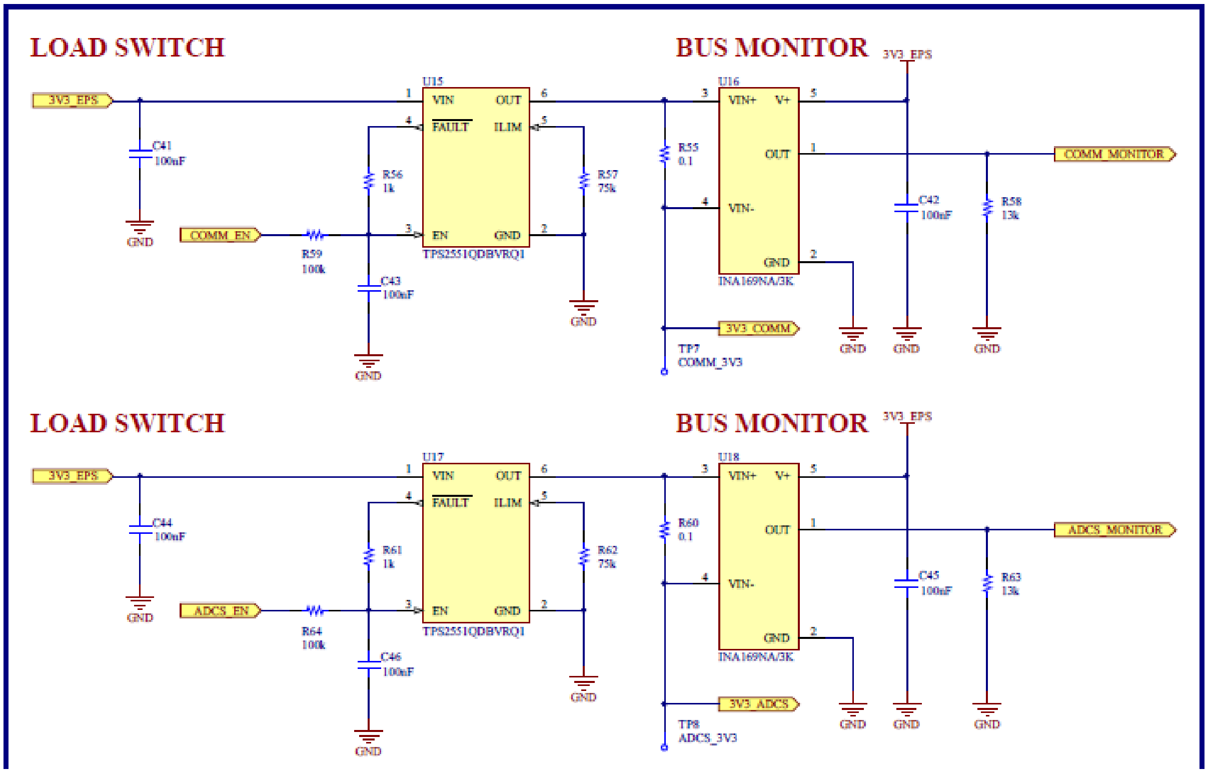
LOAD SWITCH
BUS MONITOR
3V3_EPS
U15
VIN
OUT
FAULT
ILIM
EN
GND
TPS2551QDBVRQ1
C41 100nF
COMM_EN
R59 100k
R56 1k
C43 100nF
R57 75k
U16
VIN+
V+
VIN-
INA169NA/3K
R55 0.1
3V3_COMM
TP7 COMM_3V3
C42 100nF
R58 13k
COMM_MONITOR
LOAD SWITCH
BUS MONITOR
U17
TPS2551QDBVRQ1
C44 100nF
ADCS_EN
R64 100k
R61 1k
C46 100nF
R62 75k
U18
INA169NA/3K
R60 0.1
3V3_ADCS
TP8 ADCS_3V3
C45 100nF
R63 13k
ADCS_MONITOR
GND

Figure B9. Circuit schematic of the Fault Protection Boards for the COMMS and ADCS systems [NOTE: R57 is 15 kΩ, and R62 is 36 kΩ].

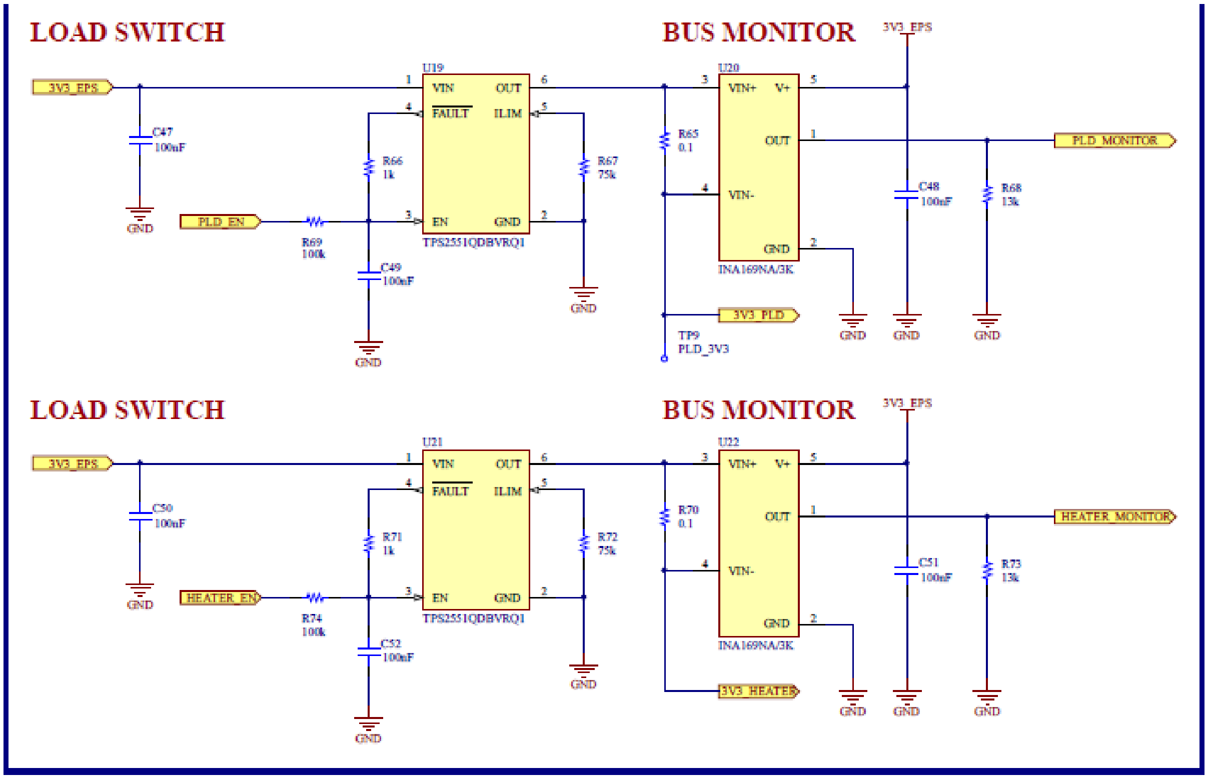
LOAD SWITCH
BUS MONITOR
3V3_EPS
U19
VIN
OUT
FAULT
ILIM
EN
GND
TPS2551QDBVRQ1
C47 100nF
PLD_EN
R69 100k
R66 1k
C49 100nF
R67 75k
U20
VIN+
V+
VIN-
INA169NA/3K
R65 0.1
3V3_PLD
TP9 PLD_3V3
C48 100nF
R68 13k
PLD_MONITOR
LOAD SWITCH
BUS MONITOR
U21
TPS2551QDBVRQ1
C50 100nF
HEATER_EN
R74 100k
R71 1k
C52 100nF
R72 75k
U22
INA169NA/3K
R70 0.1
3V3_HEATER
C51 100nF
R73 13k
HEATER_MONITOR
GND

Figure B10. Circuit schematic of the Fault Protection Boards for the Payload system and the battery heater [NOTE: R67 is 36 kΩ, and R72 is 36 kΩ]. circuit (BAT+ is the positive terminal of the on-board battery).

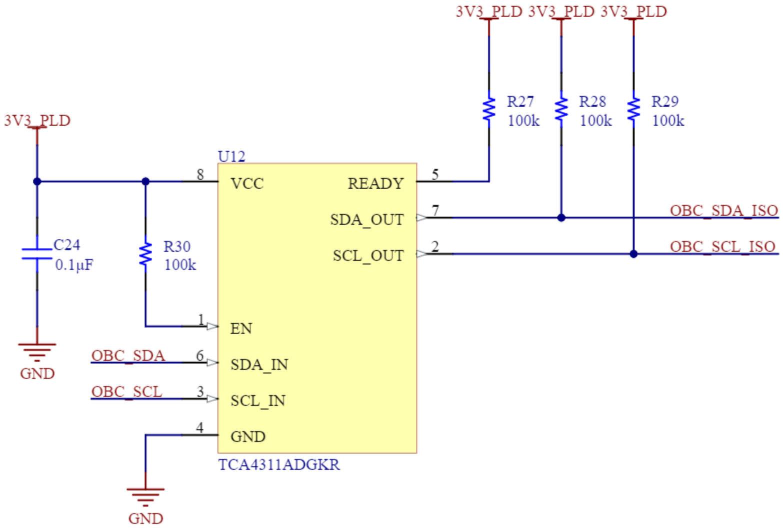
3V3_PLD
3V3_PLD
3V3_PLD
3V3_PLD
R27
100k
R28
100k
R29
100k
U12
VCC
READY
SDA_OUT
SCL_OUT
EN
SDA_IN
SCL_IN
GND
TCA4311ADGKR
8
5
7
2
1
6
3
4
C24
0.1µF
R30
100k
GND
GND
OBC_SDA
OBC_SCL
OBC_SDA_ISO
OBC_SCL_ISO

Figure B11. Circuit schematic of the I2C isolator for the Payload system. The ADCS also incorporated the same I2C isolation circuitry design [NOTE: R27-29 are 10 kΩ].

Appendix C. Battery Analysis

Table C1: Electrical Characteristics of the SparkFun Electronics PRT-08483 Batteries and the DataPower DTP 605068 Batteries

Characteristics		**PRT-0843**	**DTP 605068**
Nominal Voltage		3.7V	3.7V
Rated Capacity		2000 mAh	2000 mAh
Operating Temperature Range	Charge	0°C - 40°C	0°C - 45°C
	Discharge	-20°C - 60°C	-20°C - 60°C
Charge Current	Nominal	0.2 C (400 mA)	0.2 C (400 mA)
	Max	1 C (2000 mA)	1C (2000 mA)
Discharge Current	Nominal	0.2 C (400 mA)	0.2 C (400 mA)
	Max	2 C (4000 mA)	1C (2000 mA)
Cut-off Voltages	Charge	4.20 V	4.20 V
	Discharge	2.75 V	2.40 V
Protection Voltages (Over-discharge – Over-charge)		2.90 – 4.28 V	3.00 – 4.25 V
End-of-Charge Current		0.05 C (100 mA)	0.01 C (20 mA)
Cell Impedance		<300 mΩ	<150 mΩ
Weight		37 g	40 g
Internal configuration		Electrode stack	Electrode stack
Sealing method		Thermal scaling	Thermal scaling

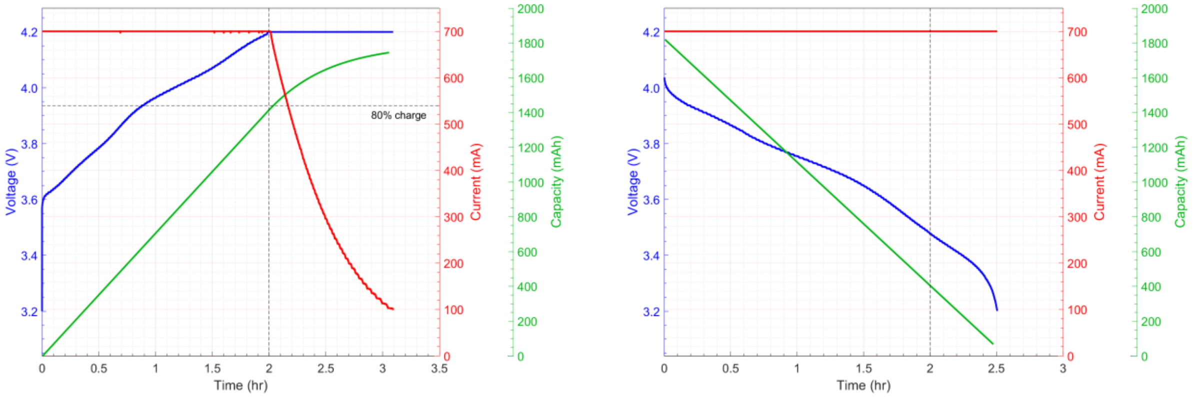

Figure C1: Left: Charge curve for a single flight Li-ion cell; Right: Discharge curve for a single flight Li-ion cell.

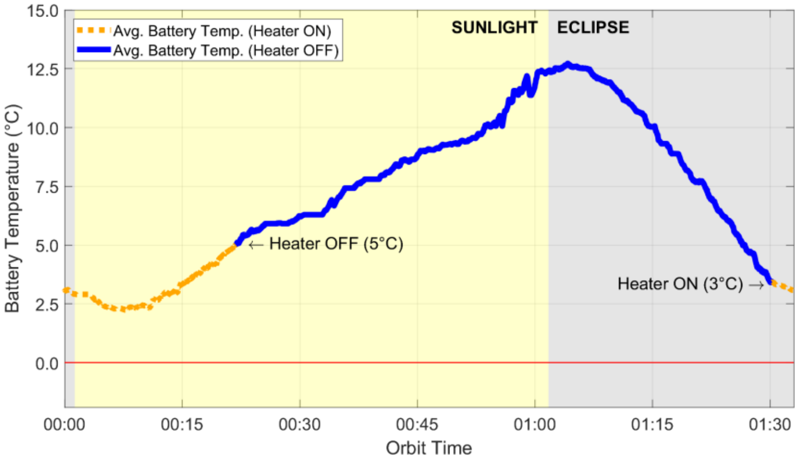

Figure C2. Typical battery thermal cycle in space (36-min eclipse).

Appendix D. Relevant EPS Design Requirements

Table D1. Key Design Requirements for Quetzal-1's Electrical Power System

Source	Type	ID	Requirement	Verification
UVG	Mission Requirements	MI-001	The satellite must incorporate a solar energy harvesting system that can provide enough power to allow the satellite to operate throughout the whole mission.	Review of design, Analysis
UVG	Mission Requirements	MI-002	The satellite must incorporate rechargeable batteries (secondary source of energy) to store the harvested solar energy.	Review of design
UVG	Mission Requirements	MI-003	The energy harvesting system must provide power surplus to the batteries to allow them to recharge after operations in umbra.	Analysis
UVG	Mission Requirements	MI-004	The batteries, along with the energy harvesting system, must be able to meet the satellite's power demand during each phase of flight.	Analysis
UVG	Design Requirements	DE-001	The satellite must incorporate an energy harvesting system composed of six solar panels and 11 solar cells.	Review of design
UVG	Design Requirements	DE-002	The EPS shall be designed in a fashion that ensures current draw will not cause solar panel brown out (0 W/0 V output).	Test
UVG	Design Requirements	DE-003	A battery heater must be implemented in order to maintain the battery cells within their operational temperature limits.	Review of design
UVG	Design Requirements	DE-004	Battery power output must be regulated to ensure that voltage requirements of every electrical component are being met.	Review of design, Test
UVG	Design Requirements	DE-005	Electronic switches must be included to turn on/off any loads when commanded by the OBC.	Review of design
UVG	Design Requirements	DE-006	The EPS must be capable of monitoring the satellite's state of health by measuring voltages, currents, and temperatures throughout the power distribution grid and reporting these variables to the OBC.	Review of design, Test
JAXA	Design Requirements	DE-007	The satellite must incorporate two or more deployment switches to keep the satellite unpowered and the battery separated from ground while the spacecraft is stowed in the deployer (JAXA, 2018).	Review of design, Test
JAXA	Design Requirements	DE-008	The stroke of each deployment switch shall be less than 2.0 mm from the surface of the rail standoffs of the satellite, and the force generated by it shall not be greater than 3 N (JAXA, 2018).	Review of design, Test
JAXA	Design Requirements	DE-009	The satellite must incorporate a Remove-Before-Flight (RBF) feature to keep the spacecraft unpowered during ground handling. The RBF must be accessible from the outside of the JAXA J-SSOD deployer once the satellite is stowed inside (JAXA, 2018).	Review of design, Test
NASA	Design Requirements	DE-010	The batteries must comply with all battery design and testing requirements specified in the JSC-20793 Crewed Space Vehicle Battery Safety Requirements Rev. D document (NASA, 2017).	Review of design, Test

Appendix E. Relevant ISS Testing Criteria for Flight Cells

Table E1: Battery Verified Characteristics List & ground test average results

Parameter	Acceptance criteria	Test results (Avg.)
Mass	Less than 0.1% change	0.017% change
Open-circuit voltage (OCV)	Less than 0.1% change	0.052% change
Capacity	Less than 5% change	1.750% change
Charge/discharge characteristic	Trend without change	No change
Discharge temperature	Trend without change	No change

Table E2: Random vibration level for battery

Frequency [Hz]	PSD [G^2Hz]
20	0.02
80	0.08
350	0.08
2000	0.014
Overall	8.6 Grms
Duration	1 min/axis